Wall Layer Microturbulence Phenomenology and a Markov Probability Model for Active Electromagnetic Control of Turbulent Boundary Layers in an Electrically Conducting Medium

J. C. S. Meng
Weapons Systems Directorate

DTIC
ELECTE
JUL 17 1995
B

19950713 045

Naval Undersea Warfare Center Division
Newport, Rhode Island

DTIC QUALITY INSPECTED 8

PREFACE

This report was prepared under Project No. M80100, "Analysis of Electromagnetic Control of Turbulence," principal investigator J.C.S. Meng (Code 801). The sponsoring activity is the Advanced Research Projects Agency (G. Jones, MSTO).

The technical reviewer for this report was P. R. Bandyopadhyay (Code 8233).

The author expresses his appreciation to W. J. Conforti (Code 0251) for his meticulous editing and technical composing, to D. P. Lavallee (Code 0252) for his patient work on illustrations and computer graphics, and to P. R. Bandyopadhyay for his technical review and comments.

Reviewed and Approved: 1 June 1995

D. F. Dence
Director, Weapons Systems

REPORT DOCUMENTATION PAGE

Form Approved
OMB No. 0704-0188

1. AGENCY USE ONLY *(Leave blank)*	2. REPORT DATE 1 June 1995	3. REPORT TYPE AND DATES COVERED

4. TITLE AND SUBTITLE

Wall Layer Microturbulence Phenomenology and a Markov Probability Model for Active Electromagnetic Control of Turbulent Boundary Layers in an Electrically Conducting Medium

5. FUNDING NUMBERS

6. AUTHOR(S)

J. C. S. Meng

7. PERFORMING ORGANIZATION NAME(S) AND ADDRESS(ES)

Naval Undersea Warfare Center Division
1176 Howell Street
Newport, RI 02841-1708

8. PERFORMING ORGANIZATION REPORT NUMBER

TR 10,434

9. SPONSORING/MONITORING AGENCY NAME(S) AND ADDRESS(ES)

Advanced Research Projects Agency
3701 North Fairfax Drive
Arlington, VA 22210

10. SPONSORING/MONITORING AGENCY REPORT NUMBER

11. SUPPLEMENTARY NOTES

12a. DISTRIBUTION/AVAILABILITY STATEMENT

Approved for public release; distribution is unlimited.

12b. DISTRIBUTION CODE

13. ABSTRACT *(Maximum 200 words)*

A thorough review of the published database on wall layer events and scales is conducted. Attention is focused on microturbulence phenomenology and the temporal and spatial scaling relationships of microturbulent events. The goal is to organize the comprehensive experimental database into a coherent framework for engineering applications to drag and noise control. The premise is that to effectively control the drag and noise in a turbulent flow, the methodology must address the genesis of the most fundamental elements of microturbulence. The Reynolds number dependence of useful parameters, such as the distance between bursts, distance between sweeps, combined ejection and burst duration, and sweep duration, is compared to verify consistency among published results on microturbulence investigations. The dynamic relationships of microturbulent burst power are derived from a heuristic perspective.

On the assumption that an electromagnetic turbulence methodology can provide a remote pressure field into the flow at the normal distance from the solid surface where most of turbulence production takes place, the threshold Lorentz pressure power is derived. This derivation is based on the principle that the pressure must equal or exceed the local, natural, turbulent burst power level to have any appreciable effect on the turbulence production process. Expressions of the ratio of Lorentz power to natural microturbulent burst power in terms of the magnetohydrodynamic (MHD) interaction parameter and electrode and magnet spacing Reynolds number are derived. Similarly, the electrode and magnet spacing Reynolds number as a function of MHD interaction parameter and length Reynolds number at threshold condition is shown. An efficiency expression for the electromagnetic control of microturbulence is obtained in terms of the MHD interaction parameter, load factor and friction coefficient, and length Reynolds number.

In search of a practical methodology to control microturbulent burst, a hypothesis is advanced that the orderly occurring microturbulent events can be considered as a Markov process, and the Markov transitional probability equations are derived for the microturbulent events. Considering the Poisson arrival rates as a representative measurable, further insights are attempted by relating the transitional probability to the experimentally obtained database on microturbulent events using either the probability density functions or the spectral densities of the shear stress and wall pressure. In light of the mathematical results, the feasibility of the Markov concept as applied generally to the active control of turbulence and specifically to the control scheme is discussed.

14. SUBJECT TERMS

Hydrodynamics	Turbulent Boundary Layers	Microturbulent Events	Turbulence Control
Electromagnetics	Magnetohydrodynamics	Lorentz Pressure Gradient	Markov Processes

15. NUMBER OF PAGES
52

16. PRICE CODE

17. SECURITY CLASSIFICATION OF REPORT Unclassified	18. SECURITY CLASSIFICATION OF THIS PAGE Unclassified	19. SECURITY CLASSIFICATION OF ABSTRACT Unclassified	20. LIMITATION OF ABSTRACT SAR

TABLE OF CONTENTS

LIST OF ILLUSTRATIONS

LIST OF TABLES

WALL LAYER MICROTURBULENCE PHENOMENOLOGY AND A MARKOV PROBABILITY MODEL FOR ACTIVE ELECTROMAGNETIC CONTROL OF TURBULENT BOUNDARY LAYERS IN AN ELECTRICALLY CONDUCTING MEDIUM

1. INTRODUCTION

In most underwater applications, performance improvement is limited by the onset or presence of turbulence. Aside from some results that can be derived through dimensional reasoning, it is still not possible to solve from the basic equations a high-Reynolds-number turbulent flow having even the simplest boundary conditions. This inability to accurately predict the parameters of turbulent boundary layers severely limits technological advancement in vehicle dynamics, including the performance of underwater propulsors and sensors.

Over the past 20 years, significant advances in flow visualization, instrumentation, and signal processing have provided a wealth of knowledge and insight into turbulent boundary flows. As has been pointed out by Cantwell (1981), there is a growing realization that turbulent flows are not totally random. The turbulence has been found to have a quasi-deterministic, repeatable pattern, as well as statistics that are characterized by a remarkable degree of order. The turbulence has been found to be composed of several identifiable events with unique characteristics; these events can be termed "microturbulent" events and their product can be termed "microturbulence." Progress in incorporating a structural model of microturbulent events into practical engineering methods, however, has been slow, and no one has yet explored how this ordered structure is to be connected with a truly predictive methodology. The investigation reported here attempts to make this connection and uses seawater electromagnetic turbulence control as a convenient practical application to test the methodology. Other turbulence control techniques could also benefit from this methodology. The overall intent is to present a new overview of the organized nature of turbulence and a road map for its control.

Turbulent boundary layer drag is dominated by the turbulence production process, which in turn is characterized by identifiable, discrete microturbulent events that have been established by numerous investigators in the past. The discrete microturbulent events are summarized in section 2 of this report, where the physical scales and sequential order of events is given in terms of the inner and outer scales of the boundary layer. Section 3 discusses the scaling relationships of these events and proposes using Lorentz pressure gradients to control the microturbulence. The complete sequence of microturbulent events occurs on a moving frame and is conceptualized as the basis of the proposed probabilistic control process. Given natural evolution, i.e., no external influence, the transition probability from one event to the next is consistent with the limiting state probabilities, with little physics to reverse the transition. When a Lorentz pressure gradient is imposed, the transition probability is modified. As proposed here, the concept of electromagnetic control of turbulence using Lorentz pressure gradients is directed at affecting the frequency of occurrence of these microturbulent events in a manner that reduces the transition probability toward the mature end of discrete events, thereby interrupting the turbulence production cycle,

reducing turbulence production and Reynolds stresses, and consequently reducing overall drag. A probabilistic model of the dependent microturbulent events is described in section 4.

Although there are global indicators of the Lorentz pressure gradient effects, to eventually provide real-time active control of the turbulent boundary layer, one must find local indicators that instantaneously characterize the Lorentz effect. Several indicators based on the wall shear stress and wall pressure fluctuations are described in section 4. Section 5 describes one method for implementing electromagnetic control of turbulence. Section 6 presents conclusions and recommendations.

2. WALL LAYER MICROTURBULENCE PHENOMENOLOGY

While a large database on wall layer microturbulence exists, the database has not been organized and presented in a comprehensive and coherent framework that lends itself to practical applications. This section offers a consolidated summary of microturbulence phenomenology with this goal in mind.

2.1 NEAR-WALL MICROTURBULENCE PHENOMENOLOGY

2.1.1 Sequence of Microturbulent Events

As is well known, Kim et al. (1971) found a quasi-periodic, three-stage sequence of events in the near-wall region of turbulent boundary layers and called the process *bursting*. This bursting is a continuous chain of events starting from a relatively quiescent wall flow; it involves the slow *lifting* of a low-speed streak, the formation of a relatively large, rapidly growing oscillatory motion, and relatively chaotic fluctuations called *breakup*. Kim et al. (1971) also found that low-speed streak-lifting is triggered by large disturbances (implying " away from the wall") already present in the flow and, hence, preceding the liftup. Corino and Brodkey (1969) found an element of accelerated fluid farther away from the wall that occurred after the appearance of a low-speed wall streak; they called this phenomenon *sweep*. Corino and Brodkey suggested that the interaction between the sweep and the low-speed streaks is fundamental to the ejection process. (Although it is recognized that streaks and near-wall longitudinal vortices are distinct dynamic elements, in this report the two terms are used interchangeably.)

Offen and Kline (1974) concluded that the beginning and growth of a disturbance in the outer flow started upstream of and prior to the appearance of a low-speed streak near the wall, and they suggested that each liftup is associated with a sweep. They affirmed that sweep—now accepted and defined as high-momentum fluid that originates in the outer layer and moves toward the wall at a relatively shallow angle—is a disturbance that originates in the logarithmic region and is characterized by a mean motion toward the wall. They suggested that such disturbances are generated by the interaction of an earlier bursting farther upstream with the fluid motion in the logarithmic region. Offen and Kline also gave a complete sequence of events: Wall disturbances grow slowly and eventually lift up. Then the velocity field is perturbed in the region directly above the oscillating wall layer. Near the end of the burst's oscillatory growth, interaction between the burst fluid and the motion in the logarithmic region causes the formation of another large vortex-like structure; this structure then creates a large wallward moving disturbance in the outer flow, which is believed to be associated with another liftup process farther downstream, thus completing the quasi-periodic sequence.

Nakagawa and Nezu (1981) focused on measuring the streamwise and vertical spatial characteristics of the ejection-sweep motions as a function of $yu_\tau/v \equiv y^+$, where y is the normal distance from the wall, u_τ is the friction velocity, and v is the kinematic viscosity; they concluded that the spatial scale of the sweeps is larger than that of the ejections and, also, that ejections

extend more widely downstream while the sweeps extend more widely upstream. Blackwelder and Eckelmann (1979) used hot-film sensors to measure both streamwise and spanwise velocity gradients as a function of spanwise dimension, and they presented a detailed map of low-speed streaking, ejection, and sweep.

Clearly, the microturbulent events depend on each other and apparently follow a quasi-periodic sequence. This experimentally observed phenomenology of the microturbulent event sequence forms the basis for the Markov analysis to be presented later.

Purtell et al. (1981) addressed the independence of the Reynolds number from the law-of-the-wall and the extent of the logarithmic region. They showed that the extent of the logarithmic region as a fraction of the boundary layer thickness does not show a decrease with Reynolds number based on the displacement thickness. They reasoned that since the hairpin eddy reflects the large-scale structure and is characterized by the extent of the logarithmic region, which is invariant with Reynolds number, the Reynolds number is independent of the large-scale structure. Head and Bandyopadhyay (1981) demonstrated the effects of the Reynolds number (over the range of $500 < Re_\theta < 17,500$) on the wall turbulence structure. They made several major points and observations. First, at low Reynolds numbers, they found that the structure is composed of vortex loops or horseshoe vortices and, with increasing Reynolds number, these structures are stretched to become elongated hairpins or vortex pairs. Second, their unique upstream- and dowstream-inclined visualization results showed that hairpin vortices, or stretched vortex loops or vortex pairs, are a major constituent of the turbulent boundary layer at all Reynolds numbers investigated and that these stretched vortex loops are substantially straight over a large proportion of their length and are inclined to the surface at a characteristic angle of 45°. Third, they found no evidence of large-scale coherent motions, other than a slow toppling or overturning motion, and they found that the large-scale structures appeared to be no more than random agglomerations of much narrower features inclined at something like 40° to 45° to the wall. Head and Bandyopadhyay suggested that these structures may have their origin in longitudinal vortex motions very close to the wall. Their observations do not change the sequence of wall microturbulent events, although they hypothesize a different picture of the wall turbulence phenomenology, namely, that the wall turbulence is a relatively ordered structure of extended vortex loops. Their remaining issue is whether the loops arise from streamwise concentration of vorticity or from the warping of transverse vorticity. This issue must await further detailed experimental analyses; it, however, has no bearing on the probabilistic model of microturbulent events to be proposed here.

As to the theoretical basis for the existence of the streaks, which are now accepted as the genesis of microturbulent events, a number of investigators have found consistent results. Bakewell and Lumley (1967) obtained a space-time correlation function of the streamwise fluctuating velocities. Using the correlation data as input to an eigen-function decomposition of the streamwise fluctuating velocity, they found a dominant large-scale structure of randomly distributed, counterrotating eddy pairs of elongated streamwise extent, similar to the commonly observed low-speed streaks visualized by wall dye layers. Later, Asai and Nishioka (1989) carried out a numerical simulation that explained the origin of the peak-valley wave structure near

4

the wall. More recently, Sabry and Liu (1991) applied a time-dependent quasi-two-dimensional formulation to simulate the formation of longitudinal vortices from initial Gortler vortices.

2.1.2 *Geometry and Kinematics of Microturbulent Events*

From their measurements of the space-time correlation of wall fluctuating velocity components, Kreplin and Eckelmann (1979) found the spanwise center-to-center spacings $\Delta z^+ \approx 50$ and streamwise length $\Delta x^+ \approx 1200$ of counterrotating vortices. Using a variable-interval time averaging (VITA) process on data from an array of hot-wire anemometers, Gupta et al. (1971) obtained detailed probability density functions (PDFs) of streak spacing over a range of Reynolds numbers and showed that the PDFs follow $\lambda^2 \exp[-(\alpha\lambda^2)]$, the Maxwell distribution, with an average $\lambda^+ \equiv \left(\dfrac{\lambda u_\tau}{\nu} \right) \approx 100$. (The PDF is further discussed later in this report.)

Kline et al. (1967) concluded that the ejection of fluid away from the wall in the subsequent process is the central mechanism for energy, momentum, and vorticity transfer between the inner and outer layers; they presented PDFs for both the spanwise and the mean spanwise spacing, with $\lambda^+ \approx 100$, and the breakups occurred in the region $10 < y^+ < 30$, with a breakup frequency F per unit span of $F^+ \equiv \left(\dfrac{F\nu^2}{u_\tau^3} \right) \approx 10^{-4}$ in the turbulent boundary layer over a flat plate with a zero pressure gradient. The characteristic frequency was measured to be $2\pi F^+ \lambda^+ = \omega^+ \equiv \left(\dfrac{\omega\nu}{u_\tau^2} \right) \approx 0.06$, which is consistent with Black's (1966) $\omega^+ \approx 0.056$ and Morrison et al.'s (1971) $\omega^+ \approx 0.07$. These characteristic frequencies can be converted to the time interval between large disturbances $\widetilde{T}_p^+ \equiv \left(\dfrac{\widetilde{T}_p u_\tau^2}{\nu} \right) \approx 100$, which is longer in comparison to the burst duration $T^+ = 20$ obtained by Kline et al. (1967). Kim et al. (1971) also presented histograms for the time interval between bursts T_B, i.e., the arrival time of the burst, and derived $T_B^+ \approx 0.65 Re_\theta^{0.73}$. Laufer and Narayanan (1970) analyzed the mean period of the turbulent production mechanism in a boundary layer and found that $U_\infty T_B / \delta \approx 5$ and is independent of Reynolds number over the range $Re_\theta = 10^3$ to 10^4. Rao et al. (1971) verified Kim et al.'s $T_B^+ \approx 0.65 Re_\theta^{0.73}$ relationship and found $T_B U_0 / \delta^* \approx 32$ independent of the Reynolds number, where U_0 is the free-stream velocity and δ^* is the displacement thickness. Bandyopadhyay (1982) showed that $U_\infty T_B / \theta \approx 8.13 A \times 10^{0.678H}$ and is dependent on the shape factor H, where A is an empirical constant. Falco (1977) reasoned the identity of "typical eddies" with Offen and Kline's "sweep," and he explained that the constancy of burst frequency across the outer region was a result of the uniform distribution of the average production of typical eddies across the outer region.

Brown and Thomas (1977) used spatial correlations of wall shear stress and streamwise velocity as a function of normal distance away from the wall to determine an oblique angle of 18° away from the wall in the streamwise direction. Their analysis was based on separating the wall

shear stress experimental data into a slowly varying part due to the large scale structure and a high frequency part due to the near-wall microturbulent bursting events. They suggested that wall shear stress fluctuation is directly connected with the bursting phenomenon, and they gave an overall conceptual model of the wall shear stress during the entire cycle from sweep to breakup to lift to a new streak. Offen and Kline (1974) showed that the sweeps are visible at $y^+ \approx 100$ and that they move at an angle of 6° relative to the plane of the wall. The 6° shallow angle is slightly greater than the 4.7° tangent angle of the $12u_\tau$ (horizontal) and u_τ (vertical) velocities well reported in the literature. Using their space-time correlation of fluctuating velocity and normal gradients, Kreplin and Ecklemann (1979) found the streamwise velocity component leading the ejected streak outward to be $\approx 13.8u_\tau$, which is essentially the mean velocity at $y^+ = 40$. Eckelmann (1974) found that the sweep traveled forward with a nearly constant velocity almost corresponding to the friction velocity u_τ. Morrison et al. (1971) measured the two-dimensional power spectra and found the characteristic near-wall streamwise and spanwise wavelengths to be $\lambda_x^+ \approx 630$ and $\lambda_z^+ \approx 135$, respectively. The $\tan \beta \equiv \lambda_z^+/\lambda_x^+ \approx 0.21$, or $\beta \approx 12°$, can be considered to be a half-angle between one upstream sweep and two downstream ejections and vice versa. Bandyopadhyay (1991) depicted the wall layer as an agglomeration of successively formed hairpin vortices arranged in a pattern with $\beta \approx 15.3°$. This overall geometry has an important implication for the control of microturbulent events. Murlis et al. (1982) showed that the burst spacing increases as y/δ decreases, indicating that near the wall the burst spacing ranges from 3δ to 5δ for $Re_\theta \approx 1880$ to 4820, where δ is the boundary layer thickness and θ is the momentum thickness.

Kim et al. measured the fraction of turbulence production during the burst period and concluded that essentially all the turbulence produced in the zone $y^+ < 100$ occurs during the burst period. Wallace et al. (1972) measured the contributions to the Reynolds stress of the inward-moving accelerated elements of fluid and the outward-moving retarded elements of fluid and reported that they are about the same. Subramanian et al. (1982) compared conditional sampling and averaging techniques in a turbulent boundary layer and found that none of the single-point detection techniques (i.e., VITA, HOLE, X-wire) was in good quantitative agreement with the rake detection technique, although qualitative agreement did exist between single-point measurements and rake measurements. More interesting is the fact that during the ejection event at $y/\delta = 0.32$ the Reynolds stress is higher than the RMS value, while during the sweep event the Reynolds stress falls below the RMS value. This fact can be very helpful in practical applications.

On wall pressure fluctuations, Schewe (1983) determined that the source of wall pressure structures is located in the buffer region of the boundary layer, the same locale where microturbulent events are taking place. The convection velocity is approximately $12u_\tau$, and the streamwise spatial scale of characteristic, large-amplitude pressure pulses is approximately $\Delta x^+ \approx 145$. Similarly, Schewe showed the pressure fluctuation frequency $\omega^+ \approx 0.52$, which is about an order of magnitude greater than what the shear stress measurement data reveal. The pressure fluctuation histogram is nearly Gaussian, indicating that it is equally likely for ejection and sweep to take place, further substantiating the hypothesis that ejection and sweep are likely to be paired in microturbulent events. This information provides insights for practical applications. Schewe

6

also determined that the pressure transducers of diameter $d^+ \equiv \left(\dfrac{du_\tau}{v}\right) \approx 20$ are required to resolve the pressure structures essential to turbulence. More recently, Löfdahl et al. (1994) showed that there was a significant increase in pressure fluctuations with $d^+ < 20$, further indicating the need for even smaller sensor diameters.

All of the above observed facts are fundamental to the thesis proposed here for the control of turbulence, viz., even though turbulent flow appears to be random and chaotic, the genesis of the turbulence is the near-wall microturbulent events, which have a remarkably quasi-periodic coherent structure, as well as deterministic, predictable statistics. By reducing the clearly identifiable microturbulent events, such as bursting and sweep frequency of occurrence, one can expect to control and reduce turbulence production. Sirmalis (1976) observed dyed turbulent boundary layers with low concentrations of polymer and found that the fine-scale turbulence was eliminated, leaving only coarse turbulence, and the boundary layer thickness was thinned. His observations are consistent with the expected effects of polymer on microturbulent events; i.e., polymer reduces the frequency of the ejection, liftup, breakup, and sweep events. In fact, this thesis has been verified by Tiederman and Luchik (1982), who injected polymer into the sublayer and found increases in λ^+ and in the time between bursts $T_B{}^+$. Using wall pressure measurement, they also established that the increase in λ^+ and $T_B{}^+$ corresponds to drag reduction.

A graphic summary of the foregoing observations is presented in figure 1, which shows an overall conceptual schematic of the wall-layer microturbulent events.

2.1.3 Relationship Between Eulerian Observation and the Lagrangian Nature of Microturbulent Events

To visualize in a Eulerian frame an event that is truly Lagrangian in nature, one must deal with the issue that definition of the sequence of events would depend on the frame of reference of observation. Based on reported experimental results, most of which are in a Eulerian frame, the microturbulent events observed in a fixed field view are the sweep, followed by oscillatory growth, and then ejection and low-speed streaks. In the Lagrangian frame, the order of sequence is reversed, i.e., ejection-growth/breakup-streaks-sweep. In a true physical sense, the Lagrangian sequence is the real sequence of events. Fundamental issues can be raised about this concept, since the microturbulent events are by no means frozen in space and simply transported by advection. However, Nakagawa and Nezu (1981) depicted a three-dimensional view of the microturbulent events occurring randomly in space and time, with the coherent structure being convected downstream in frozen-turbulence structure, therefore allowing Eulerian observation of the convecting coherent structure. Schewe (1983) also found nearly frozen structures that move with convection velocity $u_c = 12u_\tau$, also substantiating that the conceptual coherent structure repeats quasi-periodically.

In principle, any parcel of fluid evolves from one stage to another as a function of time. A continuous-dye flow visualization cannot capture any particular parcel of fluid motion evolving with time unless there is a way of tagging the different fluid parcels and tracking their motions as
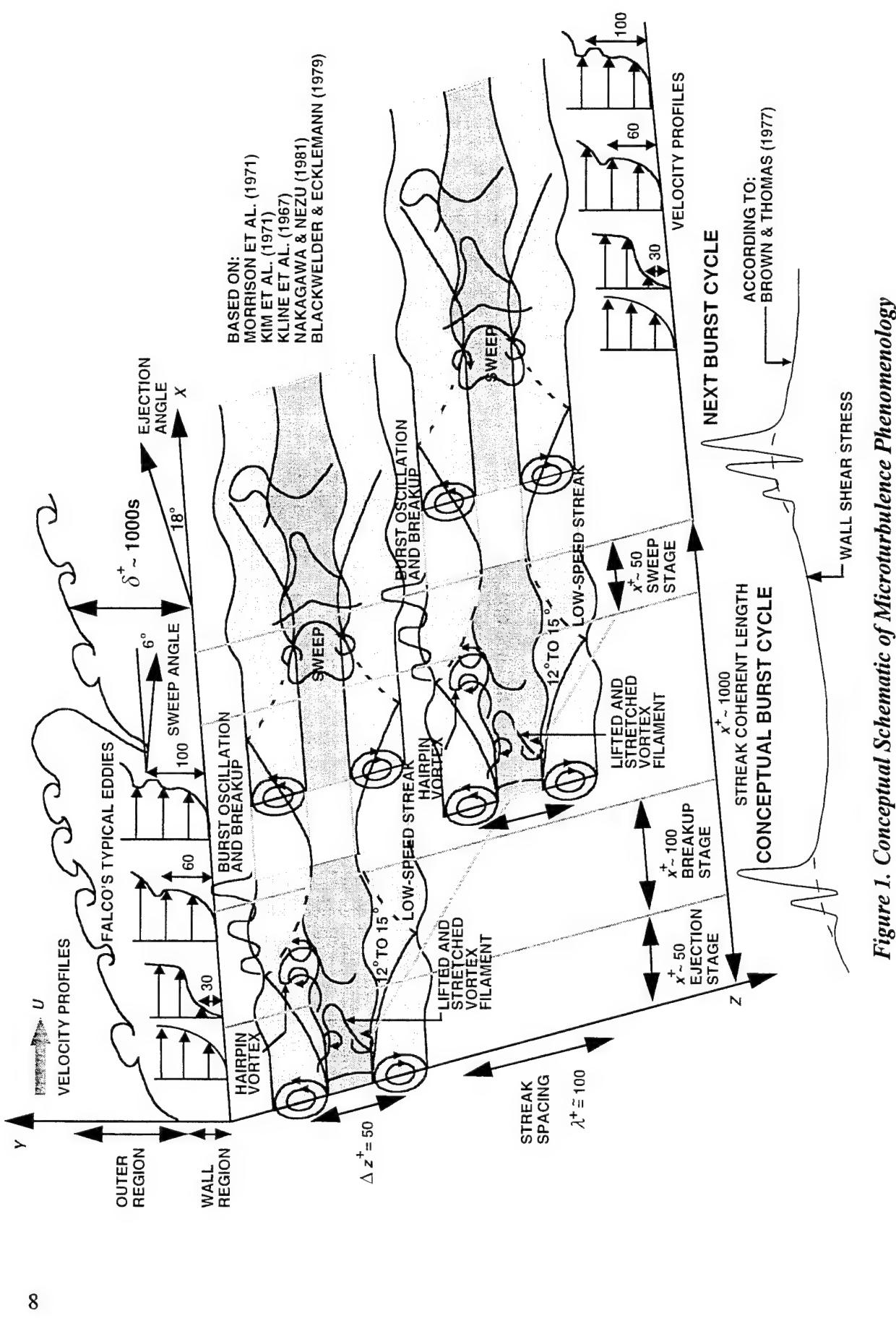
Figure 1. Conceptual Schematic of Microturbulence Phenomenology

8

a function of time. However, the continuous-dye flow visualization does capture the many events simultaneously occurring. A pulsed-dye release and continuous illumination can better provide the Lagrangian depiction of events, which is a truer representation. Unfortunately, so far no such experimental observation results have been reported.

In summary, selection of the event sequence depends on the application. For fixed point measurement and detection of microturbulent events, the relevant signal sequence is the Eulerian frame of sequence, namely, sweep-breakup/oscillatory growth-ejection-streak-sweep. This is the sequence to be addressed in the later Markov process analysis (see section 4).

2.2 SYNOPSIS OF PROBABILISTIC MODEL RESULTS OF WALL LAYER MICROTURBULENT EVENTS

2.2.1 Microturbulence PDFs

Based on visualization results, Nakagawa and Nezu (1977) stated that the probability of the occurrence of the streak spacing follows a log-normal distribution. Smith and Metzler (1983), employing hydrogen bubble wire flow visualization, confirmed this log-normal distribution of the streak spacing, instead of the Maxwell distribution of Blackwelder and Eckelmann (1979). Smith and Metzler stated that the streaks maintain their integrity and reinforce themselves for time periods up to an order of magnitude longer than the observed burst periods.

Kim et al. (1971) obtained histograms of burst frequency versus y^+ and established that there is a close association with the turbulence production versus y^+ and that both distributions appear to be similar to a Rayleigh distribution. Rao et al. (1971) suggested that the time between bursts follows a log-normal distribution. Bark (1975) applied Rao et al.'s (1971) results of the log-normal law of the time between bursts and assumed that the temporal and spatial structure is the same for all bursts, with the strengths following a Poisson distribution.

Murlis et al. (1982) obtained the conditional PDFs of turbulent zone lengths in the intermittent region; this intermittent turbulent zone length can be a qualitative representation of the burst's streamwise dimension. The peak PDF zone length $L^+ \approx 120$, which is half the length of a typical eddy, can be considered the most probable burst length and was found to be independent of Reynolds number. The burst length PDF appears, to the present author, to follow an Erlang distribution.

Eckelmann (1974) presented the PDF of streamwise velocity, which is highly asymmetric near the wall. Mitchell and Hanratty (1966), who used an electrochemical wall shear stress meter in a pipe flow, obtained the PDF for the axial velocity over the entire velocity range and showed that it has a near-Gaussian distribution, with a small skewness toward higher velocity. Bark's energy spectra of the streamwise velocity fluctuations were in agreement with measurements by Morrison et al. (1971). Using a nine-sensor hot-wire vorticity meter, Vukoslavcevic et al. (1991) measured the PDF of three vorticity fluctuations and showed that the spanwise component in the near-wall region, as close to the wall as $y^+ = 11.1$, is quite negatively skewed, indicating that

9

intense spanwise vorticity stretching predominates over vorticity compression there. Their results also show that the velocity and wall pressure spectra are very similar.

Sreenivasan and Antonia (1977) presented the normalized wall shear stress PDF and showed that it is not Gaussian. They also compared the normalized power spectral density of wall shear stress versus frequency obtained by a number of measurements. Schewe (1983) verified the histogram of wall pressure fluctuation to be very nearly Gaussian, indicating that wall pressure fluctuations encompass effects from both near-wall motions and large-scale motions away from the wall. From a statistical modeling point of view, this means that the wall pressure PDF is the convolution of many PDFs of many preceding events and, therefore, should follow a Gaussian distribution. Blake (1970) obtained the $p'^2/q \sim 3.4 C_f$, where $q = 1/2 \rho U_0^2$, over a range of Reynolds numbers from 8000 to 28,000; this relationship can also be used to calibrate the wall pressure and shear stress measurements.

2.2.2 *Probabilistic Models of Microturbulent Events*

Inspired by Kim et al.'s results, Kovasznay (1975) proposed a model of linear superposition of randomly distributed deterministic structures with a Poisson distribution of arrival statistics. Bark (1975) derived a probabilistic model of the turbulent stresses based on a random system of bursts using an idealized model of the joint probability distribution in time and space of the occurrence of bursts. Unfortunately, no further development of similar models followed. The known mathematical significance of the Rayleigh probability distribution, the ubiquitous log-normal distribution (see for example Aitchison and Brown (1957)), the Poisson distribution, and the normal distribution can be applied to infer a possible functional relationship among the random variables. Such a relationship may offer additional insight into interpretation of the experimental data, which is the focus of this section.

It is well known that if two random variables x and y are normal and independent with zero mean and equal variance, then the random variable $z = \sqrt{(x^2 + y^2)}$ follows a Rayleigh distribution. If the random variable x follows a normal distribution, then the variable $z = e^x$ follows a log-normal distribution. A log-normal distribution also indicates that the random variable's variations are proportional to the variable itself. If two random variables are Poisson-distributed with parameters λ and μ, then their sum is also Poisson-distributed with parameters $\lambda + \mu$. If two random variables are normal-distributed, then their sum is also normal-distributed. By the central limit theorem, the sum of multiple random variables of any distribution will nearly follow a normal distribution. It is useful to apply these facts to interpret the microturbulence PDFs.

Table 1 summarizes the known PDFs of microturbulent random variables as an aid to inferring possible relationships among them. As can be seen, the wall shear stress—which is the sum of shear stresses in the streamwise and spanwise directions—follows a Rayleigh distribution. The low-speed streak spacing, the time between bursts, and the time between sweeps follow a log-normal distribution, while the burst length in the intermittent region follows an Erlang distribution. Random variables that follow a normal distribution are the axial velocity and its normal gradient, the spanwise velocity and its normal gradient, and the wall pressure fluctuations.

10

In the discussion that follows, several examples of experimental observations and probabilistic interpretations of the relationship among these random variables are given to illustrate the insight a probabilistic model can offer.

Table 1. Known PDFs of Microturbulent Random Variables

Generic PDF			
Rayleigh	Erlang	Log-Normal	Gaussian (Normal)
Frequency of burst vs y^+ Turbulence production vs y^+ Wall shear stress	Burst length in the intermittent region	Low-speed streak spacing Time between bursts Time between sweeps	Axial velocity and normal gradient at $y^+ \cong 3$ Spanwise velocity and normal gradient at $y^+ = 2.7$ and 5.1 Wall pressure fluctuations

Figure 2 illustrates the fact that the low-speed streak spacing follows a log-normal distribution. The experimental data and the fact that the spacing follows a log-normal distribution were obtained by Smith and Metzler (1983). The mean streak spacing in terms of wall units is approximately 100. The probabilistic meaning of the streak spacing following a log-normal distribution can be traced to the fact that the spacing is approximately twice the cylindrical vortex core radius. The core radius is inversely proportional to the spanwise cellular motion velocity, which is proportional to the distance from wall. In other words, the fluctuation of low-speed streak spacing is proportional to the spacing itself; thus, its PDF should follow a log-normal distribution.

Figure 3 compares experimental data for the time interval between bursts; it shows, along with a log-normal distribution, data from Kim et al. (1971) for $Re_\theta = 660$ and 1100, and data from Rao et al. (1971) for $Re_\theta = 620$. Among several distributions tried—Erlang, Maxwell, Rayleigh and log-normal, the log-normal distribution provided the best fit to the data. Only the distribution best fitted to the Kim et al. data with $Re_\theta = 1100$ is shown here; a better fit to the other two data sets can be obtained, but it was deemed not necessary for the purposes of this report. It can be reasoned that T_B, which describes the time interval between two arrivals, should follow an Erlang distribution with $n = 2$. The data clearly indicate that this is not the case, implying that a scenario with bursts arriving perhaps from neighboring ailes of microturbulent events dominates the arrivals, rather than the conceptual scenario of an orderly advection of bursts from upstream.

11
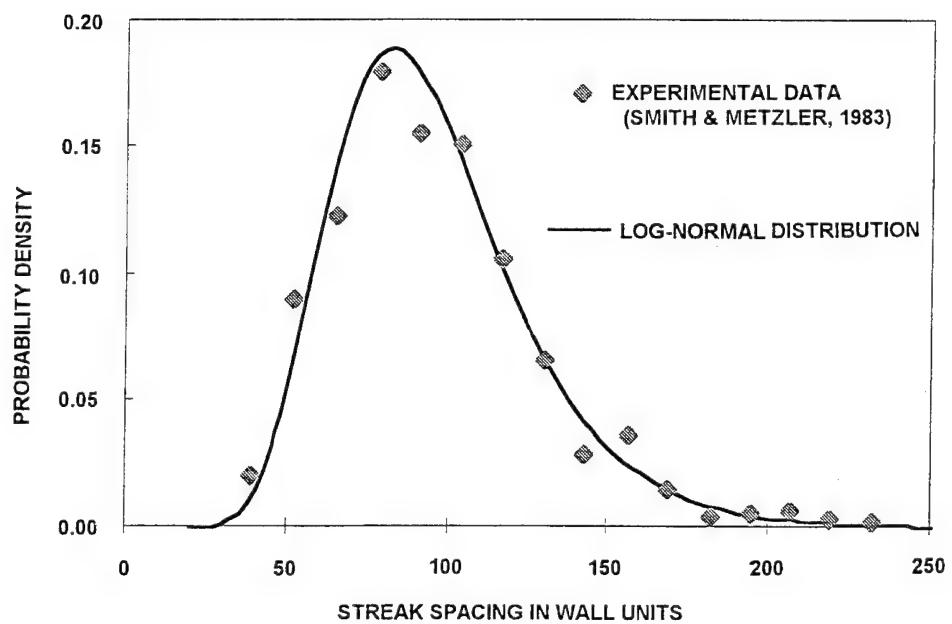
Figure 2. Probability Density Function of Streak Spacing
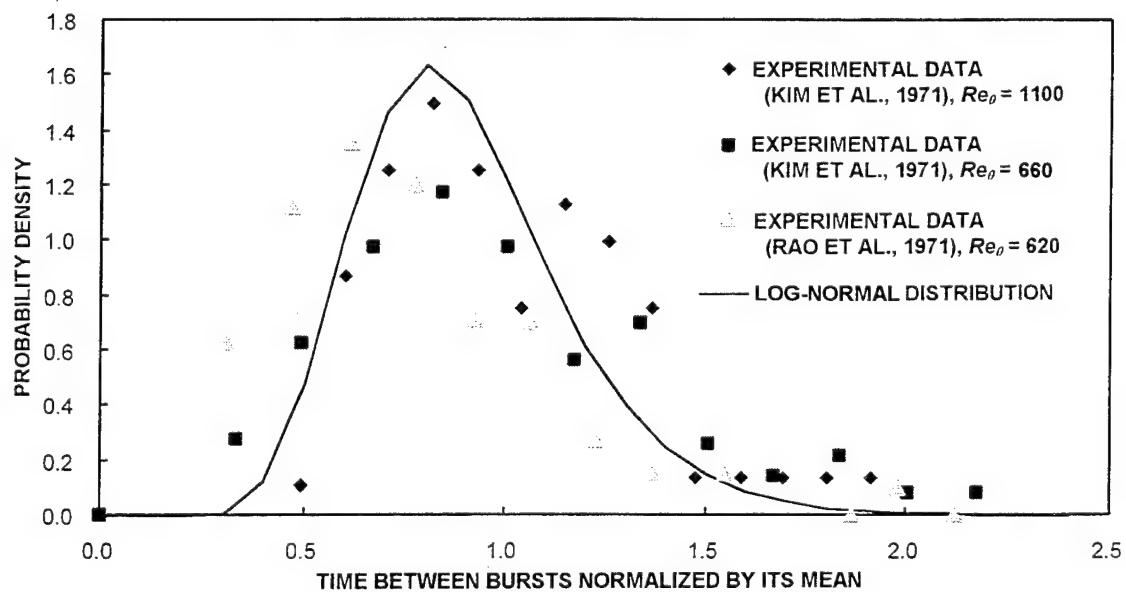
Figure 3. Probability Density Function of Time Between Bursts

Figure 4 compares the instantaneous streamwise velocity PDF obtained by Eckelmann (1974) with a log-normal distribution. These data were analyzed and interpreted for their probabilistic meaning. Here the data have been normalized by the local mean streamwise velocity to allow comparison of velocities from two y^+ heights (2.7 and 5.1), and the best fit was found to be a log-normal distribution. Since the mean streamwise velocity in the wall region is known to vary linearly with distance y^+, the streamwise velocity fluctuation also varies with the local streamwise velocity; thus, its PDF should follow a log-normal distribution.
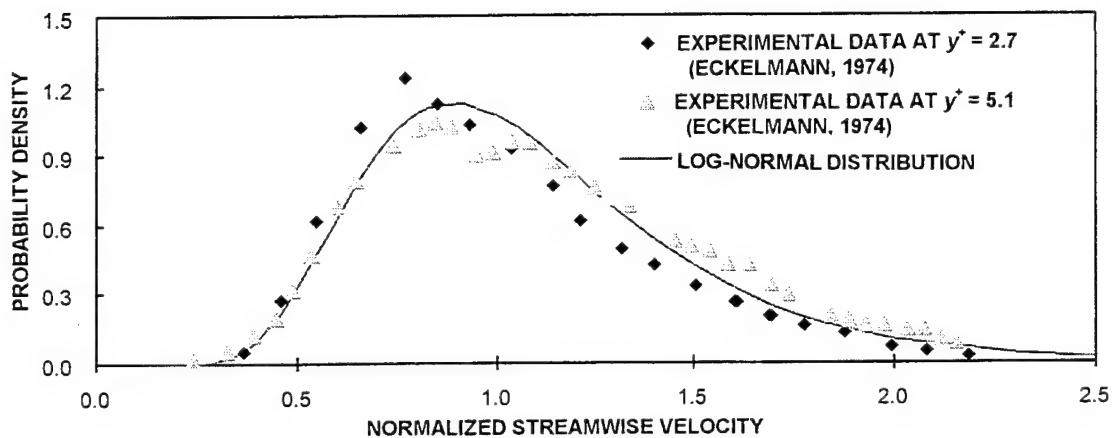
Figure 4. Probability Density Function of Instantaneous Streamwise Velocity Normalized by Local Mean Velocity

Figure 5, from Murlis et al. (1982), shows experimental data for the burst length in the intermittent region, along with an Erlang distribution. Since the burst length can be interpreted as the distance between ejection and sweep, it is therefore the renewal process length from the arrival of ejection to the end of sweep. The arrival of ejection and sweep can be conceived as random variables following a Poisson process; thus, the burst length in the intermittent region should follow an Erlang distribution of order $n = 2$. As is shown in figure 5, the experimental data reasonably follow an Erlang distribution, illustrating the plausibility of a Poisson process for the ejection and sweep events, so that one can experimentally determine the arrival rate of each event that is near the wall and hence be able to predict the burst length in the outer (intermittent) region away from the wall.

In figure 6, experimental data for the wall shear stress (from Sreenivasan and Antonia, 1977) are shown, together with a Rayleigh distribution. The data again reasonably conform to a Rayleigh distribution, although one can probably find a closer fit than that shown. Since, as has been demonstrated by Vukoslavcevic et al. (1991), the streamwise shear stress $\partial u/\partial y$ and the

13
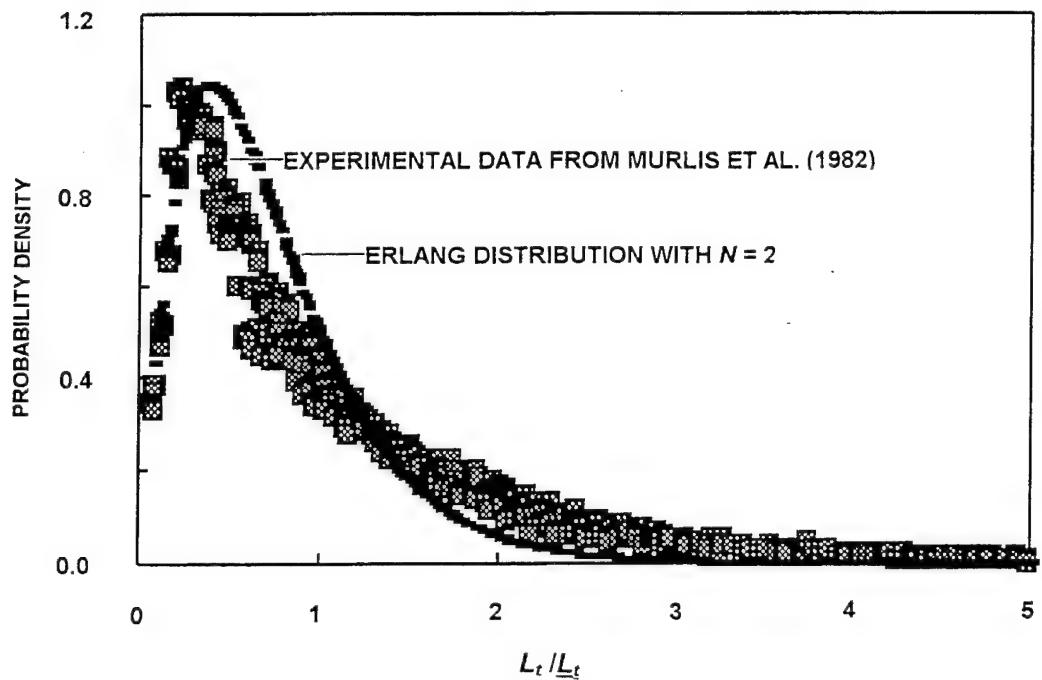
*Figure 5. Probability Density Fucntion of Burst Length
Compared with Erlang Distribution*
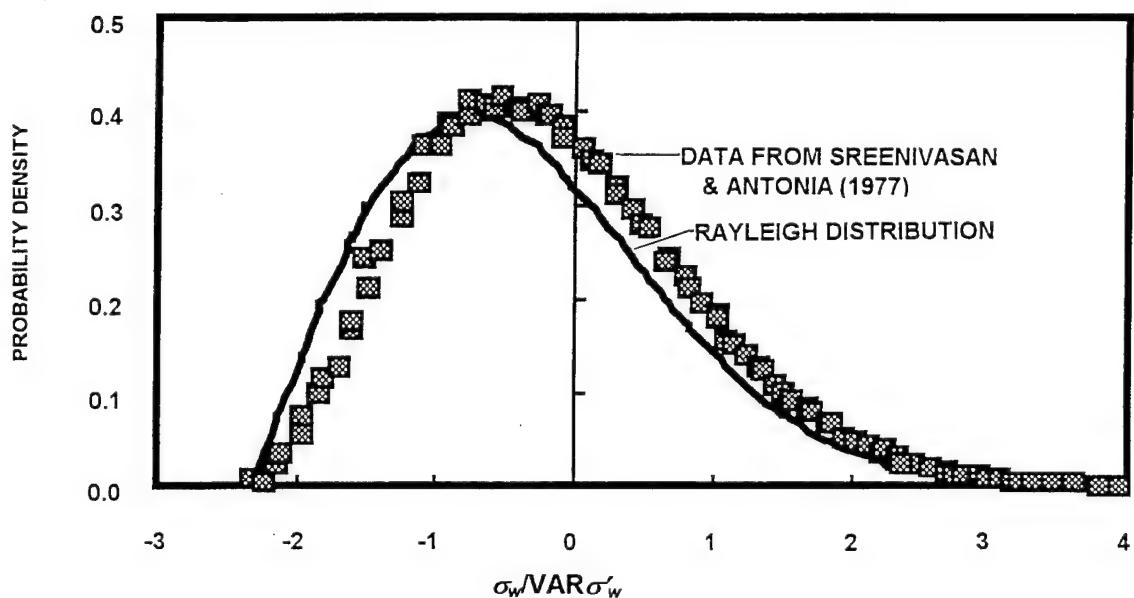
*Figure 6. Probability Density Function of Wall Shear Stress
Compared with Rayleigh Distribution*

14

spanwise stress $\partial w/\partial z$ both follow nearly normal distributions, and the wall shear stress is the square root of the sum of the squares of the streamwise and spanwise components, it is expected from probability theory that the wall shear stress should nearly follow a Rayleigh distribution as figure 6 shows. Antonia and VanAtta (1977) showed that the Gaussianity of the velocity fluctuations is valid only as close to the wall as to $y/\delta \approx 0.1$, and that the spectrum of the Reynolds stress can be derived from the Gaussianity assumption.

Figure 7 compares the experimental data of wall pressure fluctuations obtained by Schewe (1983) with a Gaussian distribution. The fit is exceedingly good, as is expected from the incompressibility of the fluid. The elliptic nature of the governing Poisson equation dictates that the wall pressure fluctuations be a result of disturbances over a domain of influence significantly larger than the wall shear stress counterpart, so that it is a sum of many random variables; therefore, its PDF follows a Gaussian distribution.
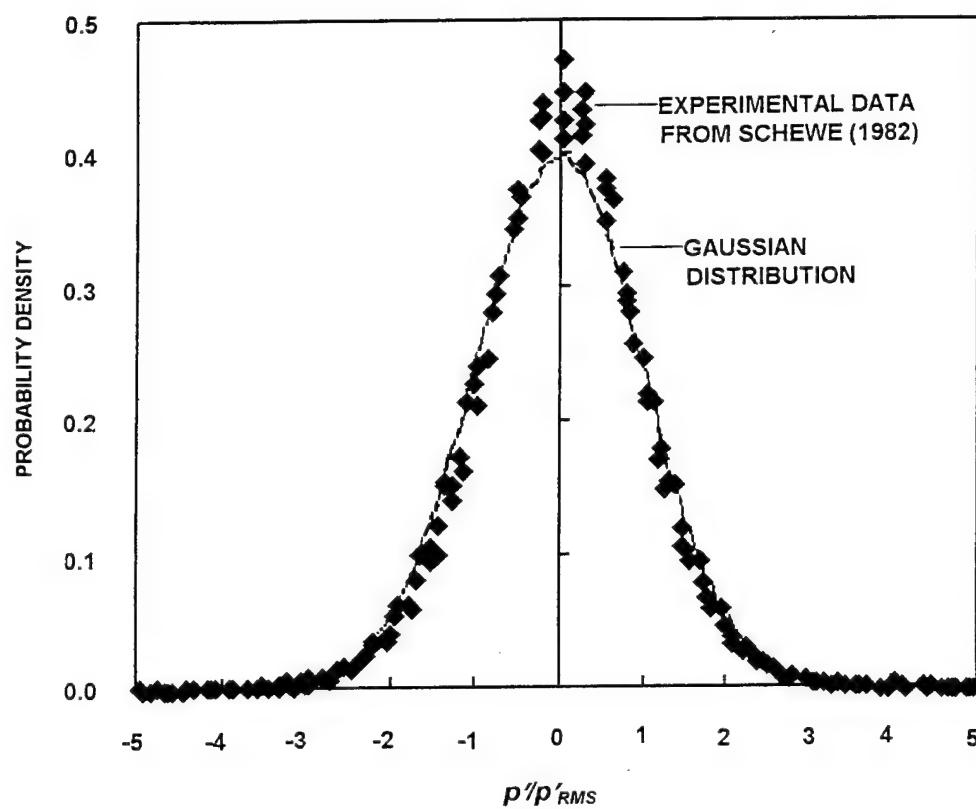
Figure 7. Probability Density Function of Wall Pressure Fluctuation Compared with Gaussian Distribution

15

2.2.3 Probabilistic Model and Electromagnetic Turbulence Control

Based on the above experimentally observed PDFs and the sequence of microturbulent events, one can construct a conceptual probabilistic model of dependent random variables. The model starts with the low-speed streak spacing, which has a log-normal distribution; then, the liftups take place with a frequency PDF of Rayleigh distribution, followed by another Rayleigh distribution of the sweeps, and a log-normal distribution of the mean time between bursts. Each microturbulent event contributes to the wall shear stress; the low-speed streak contributes at the low end, with the liftup less than the mean and the sweeps greater than the mean, so that the wall shear stress PDF can be construed as the weighted sum of the individual PDFs. This wall shear stress PDF can be compared with the measured PDF to " fine tune" the weighting factors for practical applications. Similarly, the contributions from each microturbulent event to the wall pressure fluctuations can be estimated in the same manner.

The weighting factors thus derived correlate to the percentages of time of each natural microturbulent state. When external electromagnetic influences are present, however, the weighting factors will vary because the electromagnetic influences will inhibit certain events (such as liftup and bursting), thereby reducing turbulence production, and will promote other events (such as the low-speed streaks, which contribute to lower shear stress), thereby reducing the total drag over time.

In summary, the observed quasi-periodic nature of coherent microturbulent events that are taking place randomly in a spatial dimension near the wall can be applied to predict the next microturbulent event, thereby offering an opportunity to activate an opposing remote Lorentz pressure gradient to inhibit the turbulence production process. In other words, the turbulence control is based on applying Lorentz pressure gradients toward the wall during predicted liftup, Lorentz pressure gradients away from the wall during predicted sweep, and no pressure gradients during the low-speed streak. This is the fundamental basis of estimator-predictor feedback control of turbulence based on the known, dependent, random microturbulent event processes. By sampling the wall shear stress and pressure fluctuations and obtaining a real-time solution based on the Markov probabilistic model, the microturbulent state can be predicted and the Lorentz pressure gradients applied, which should result in the total turbulent drag being reduced.

The principles of electromagnetic turbulence control are to apply the Lorentz pressure gradient at the normal distance from the wall where the peak turbulence production occurs naturally. The objective is not to totally eliminate turbulence but only to inhibit turbulent ejection and sweep, allowing the low-speed streaks to exist and persist since they contribute to a more naturally stable mode of flow near the wall and are responsible for a low level of shear stress and therefore skin friction drag.

Figure 8 illustrates the concept of applying Lorentz pressure gradient vectors to inhibit the naturally occurring microturbulent events. It shows the idealized Lorentz pressure gradient vectors inhibiting ejection and sweep simultaneously.
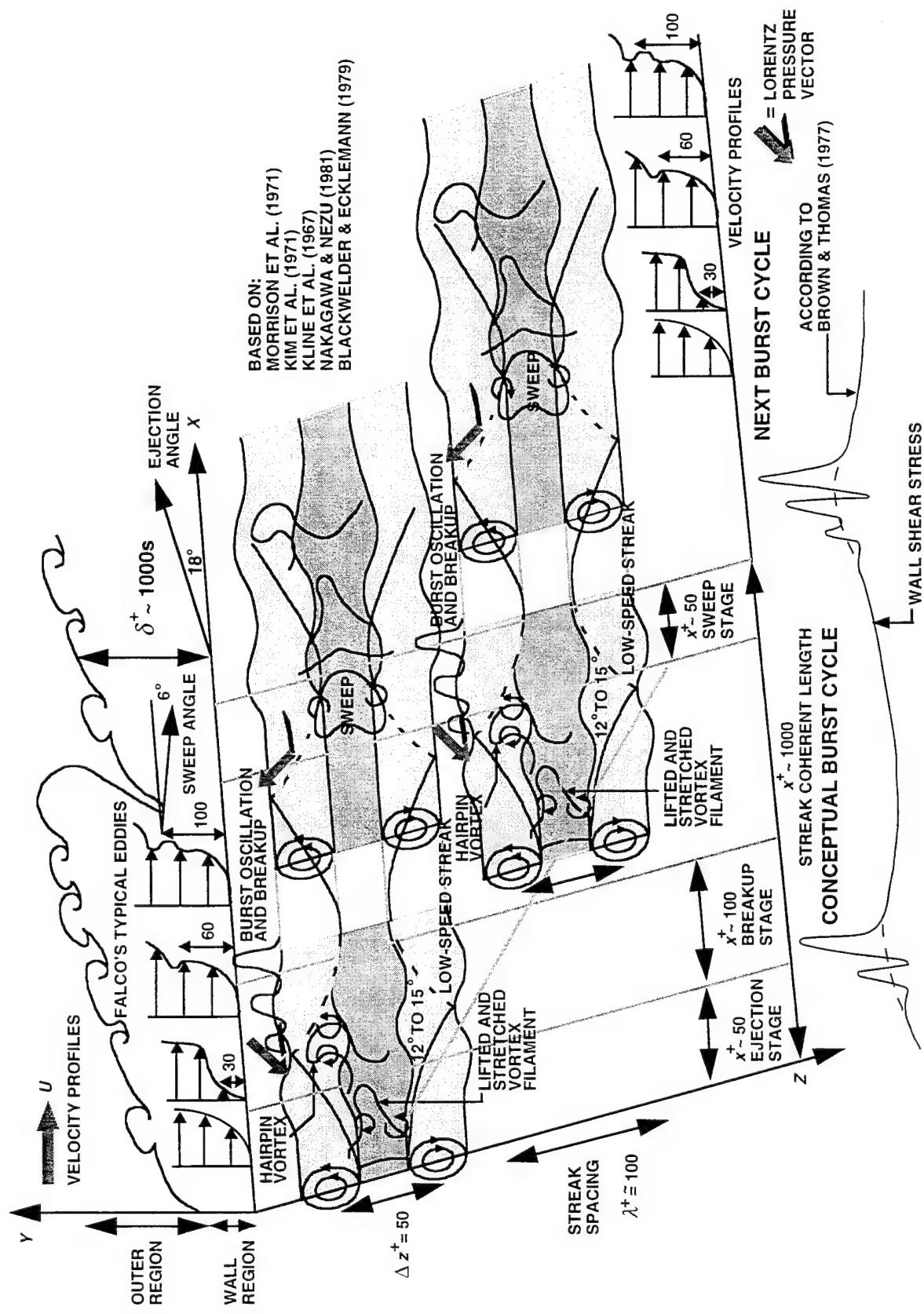
Figure 8. Application of Lorentz Pressure Gradient Vectors to Inhibit Microturbulent Events

3. SCALING RELATIONSHIPS OF MICROTURBULENT EVENTS

3.1 KINEMATIC PARAMETERS

Table 2 presents a detailed comparison of the scales of wall turbulence. As can be seen, the microburst event has attracted the most attention from investigators because the largest part of the total Reynolds stress is produced during the short burst periods (Corino and Brodkey, 1969). From this table, one can compile and extract a number of important microturbulent event scales for later dynamic analysis. First are the dimensionless scales of microturbulent events (see figure 9). Note the reasonable agreement between the two curves for *dimensionless distance between bursts* (these are from Subramanian (1982) and Lu and Willmarth (1973)). Both yield similar trends and are on the same order of magnitude as the well-known correlation length of the wall layer low-speed streaks. The dimensionless duration of ejection and bursting is $0.8\delta^*/U_\infty$, as given in table 2 (Lu and Willmarth, 1973). Similarly, the time period between bursts is given by Lu and Willmarth (1973). It is important to note that the burst period is about 70 times longer
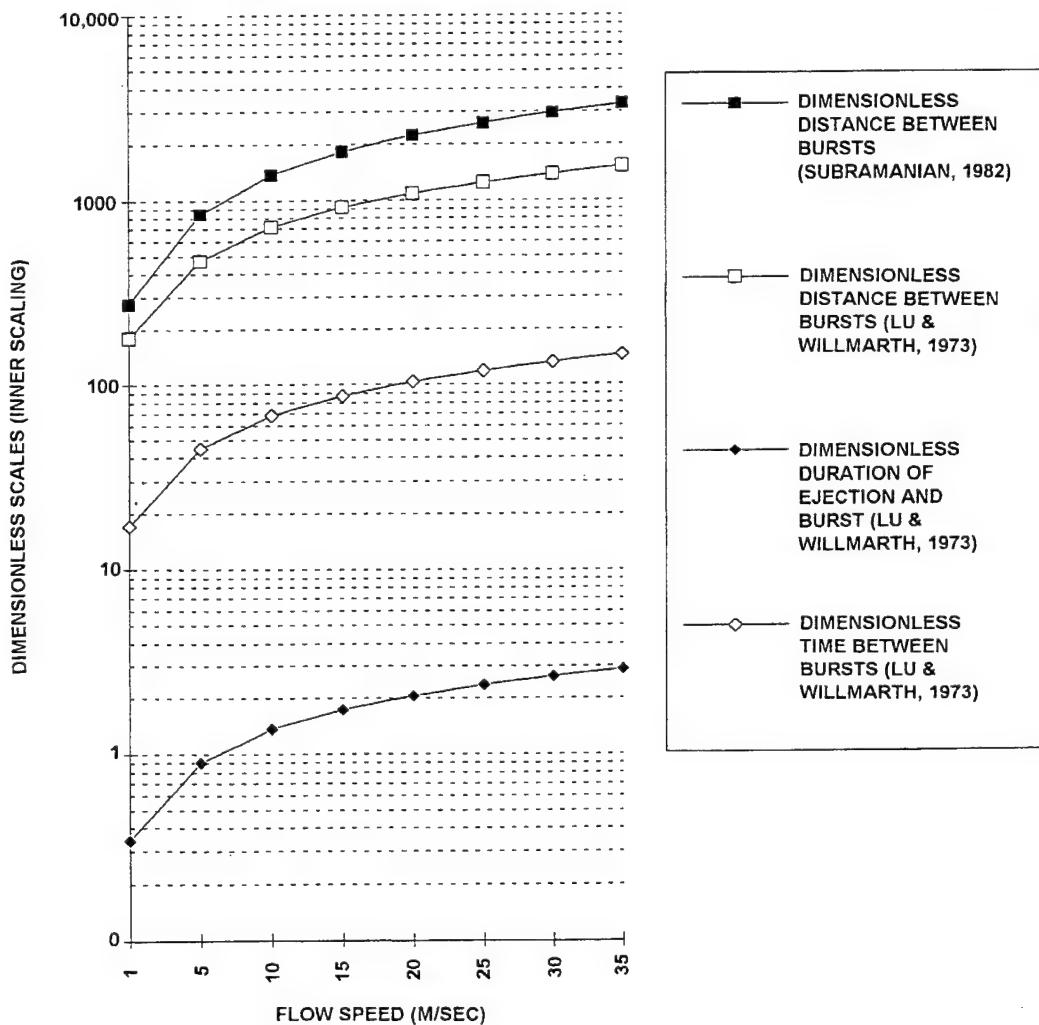
Figure 9. Dimensionless Time and Length Scales vs Flow Speed

19

Table 2. Scales of Wall Turbulence

Flow Regime→	Transitional	Turbulent Wall Region — Kline's Burst Cycle (1967)				Turbulent Outer Region	
Events→ / Mean Scales	Spot	Streak	Ejection (Streak-Lifting)	Bursting (Oscillatory Growth and Breakup)	Sweep	Typical Eddy	Large-Scale Motion
Streamwise Length (x^+)	2 to 4δ	1 to 2δ $(1200)^{[a]}$	0.1 to $0.2\delta^*$ (20 - 40)	0.2 to $0.5\delta^*$ (40 - 150) $(120)^{[b]}$	0.1 to $0.3\delta^*$ (20 to 90)	0.25δ (<200)	1.6 to $4\delta^*$
Spanwise Length (z^+)	2 to 4δ	(100) $\sigma \cong 0.4$	(5 to 50)$^{[c]}$ (10 to 30)$^{[d]}$	(<100)	(<100)	(200)	0.5 to $1\delta^*$
Normal Distance from Wall (y^+)	δ (500)	(0 to 30) (center @ 20 - 30)	(15 to 20)	(15 to 60)	(<100)	$\leq\delta$ (100) (edge of turbulent/ irrotational flow interface)	δ
Time Duration (Interval)	Indefinite	480 up to 2500$^{[e]}$ $(F^+\lambda^+)^{-1} \cong 100$	$0.2\dfrac{\delta^*}{U_\infty}$	$0.6\dfrac{\delta^*}{U_\infty}, T^+ = 20$ $\left(32\dfrac{\delta^*}{U_\infty}, 6\dfrac{\delta}{U_\infty}\right)$ $\left(T_B\dfrac{u_\tau^2}{\nu} = 0.65Re_\theta^{\,0.73}\right)^{[f]}$	$0.3\dfrac{\delta^*}{U_\infty}$, $T^+ \cong 20$ $(40\dfrac{\delta^*}{U_\infty})$	N.A.	$2.5\dfrac{\delta^*}{u_\infty}$
Burst Rate per Span (F)	N.A.	N.A.	---	$1.5 \times 10^{-4}\ @\ \dfrac{dp}{dx} = 0$	---	---	---
Advection Velocity in U_∞ (u^+)	0.5 to 0.8	N.A.	0.4 to 0.8 (12)	0.4 to 0.8 (12)	0.4 to 0.8 (12)	0.95	0.95
Vorticity Strength	$\dfrac{U_\infty}{\delta^*}$ to $\dfrac{u_\tau^2}{\nu}$	$0.1\dfrac{u_\tau^2}{\nu}$	N.A.	$1.2\dfrac{u_\tau^2}{\nu}$	$\dfrac{u_\tau^2}{\nu}$	$0.4\dfrac{u_\tau^2}{\nu}$	$\dfrac{U_\infty}{\delta^*}$
References	Wygnanski et al. (1976); Cantwell et al. (1978)	Kline et al. (1967); Blackwelder & Eckelmann (1976); [a]Kreplin & Eckelmann (1979); [e]Smith & Metzler (1983)	Kline et al. (1967) [c]Corino & Brodkey (1969); [d]Kim et al. (1971)	Kline et al. (1967); Kim et al. (1971); [f]Rao et al. (1971) Lu & Willmarth (1973); Blackwelder & Eckelmann (1979); Kreplin & Eckelmann (1979); [b]Murlis et al. (1982);	Kim et al. (1971); Lu & Willmarth (1973)	Falco (1977); Head & Bandyopadhyay (1981)	Falco (1977)

N.A. = Not Applicable.

20

than the duration of ejection and bursting. Because of the microscales of the turbulent events, it is conceivably more difficult to inhibit each individual ejection and bursting over a small spatial scale and short temporal scale. Conceptually, the electromagnetic turbulence control (EMTC) pulse rate should be based on the burst period rather than on the individual ejection and burst durations.

3.1.1 Time Scales

From Corino and Brodkey (1969), the combined ejection-breakup duration can be calculated to be $0.8\delta*/U_\infty$, which can be expressed in terms of inner scaling as $0.00136Re_x^{0.6}$, where Re_x is the streamwise length Reynolds number. Similarly, the sweep duration in terms of inner scaling can be expressed as $5.1 \times 10^{-4}Re_x^{0.6}$. The burst period is $30\delta*/U_\infty$ or, in terms of inner scaling, $0.051Re_x^{0.6}$. Figure 10 illustrates the time scales in dimensional form. As flow speed increases for the same length x, the ejection-breakup and sweep durations decrease inversely as $Re_x^{-1.4}$, and the frequency increases as $Re_x^{1.4}$.
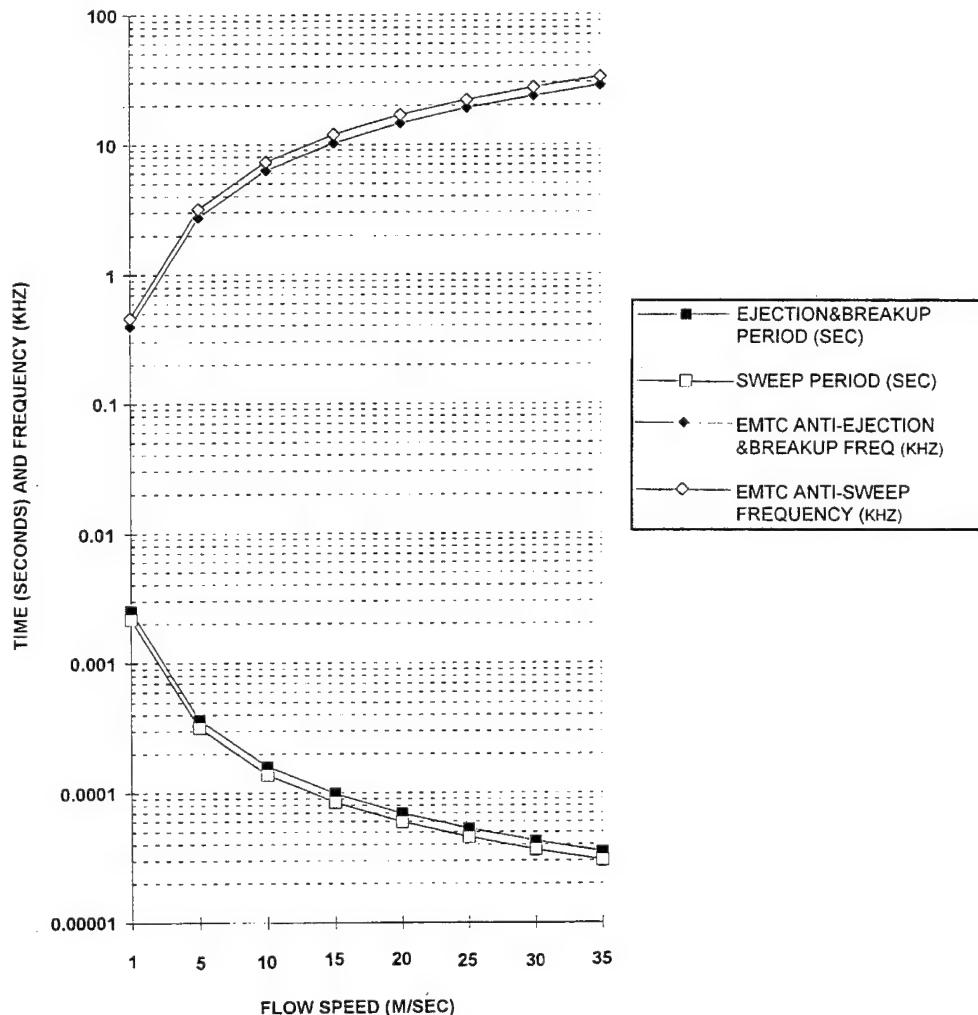
Figure 10. Dimensional Time Scales vs Flow Speed

21

3.1.2 Length Scales

Dimensionless length scales have been provided by several investigators. As indicated in table 2, the combined ejection and burst length scales can be obtained by multiplying the combined ejection and burst duration by the local streamwise velocity at $y^+ = 40$. The local velocity is calculated from the van Driest formula: $u^+ = 5.5 \log y^+ + 5.2 = 14$. While one could question the Reynolds number dependence of these relationships, Purtell et al. (1981) established that, at least in the low-Reynolds number range, the law-of-the-wall and the extent of the logarithmic region are independent of the Reynolds number. Therefore, in terms of inner scaling, the combined ejection and breakup length is 11.2 $\delta^* u_\tau / U_\infty$ or $0.0191 Re_x^{0.6}$. Similarly, the burst's periodic length can be calculated to be 420 $\delta^* u_\tau / U_\infty$ or, in terms of inner scaling, $0.7148 Re_x^{0.6}$. Lu and Willmarth (1973) also gave the burst's periodic length to be 4.3δ, which translates to $0.4327 Re_x^{0.7}$, which is not very different from the expression above over the range of validity of $5 \times 10^5 < Re_x < 10^7$. These scales are illustrated in figure 11.
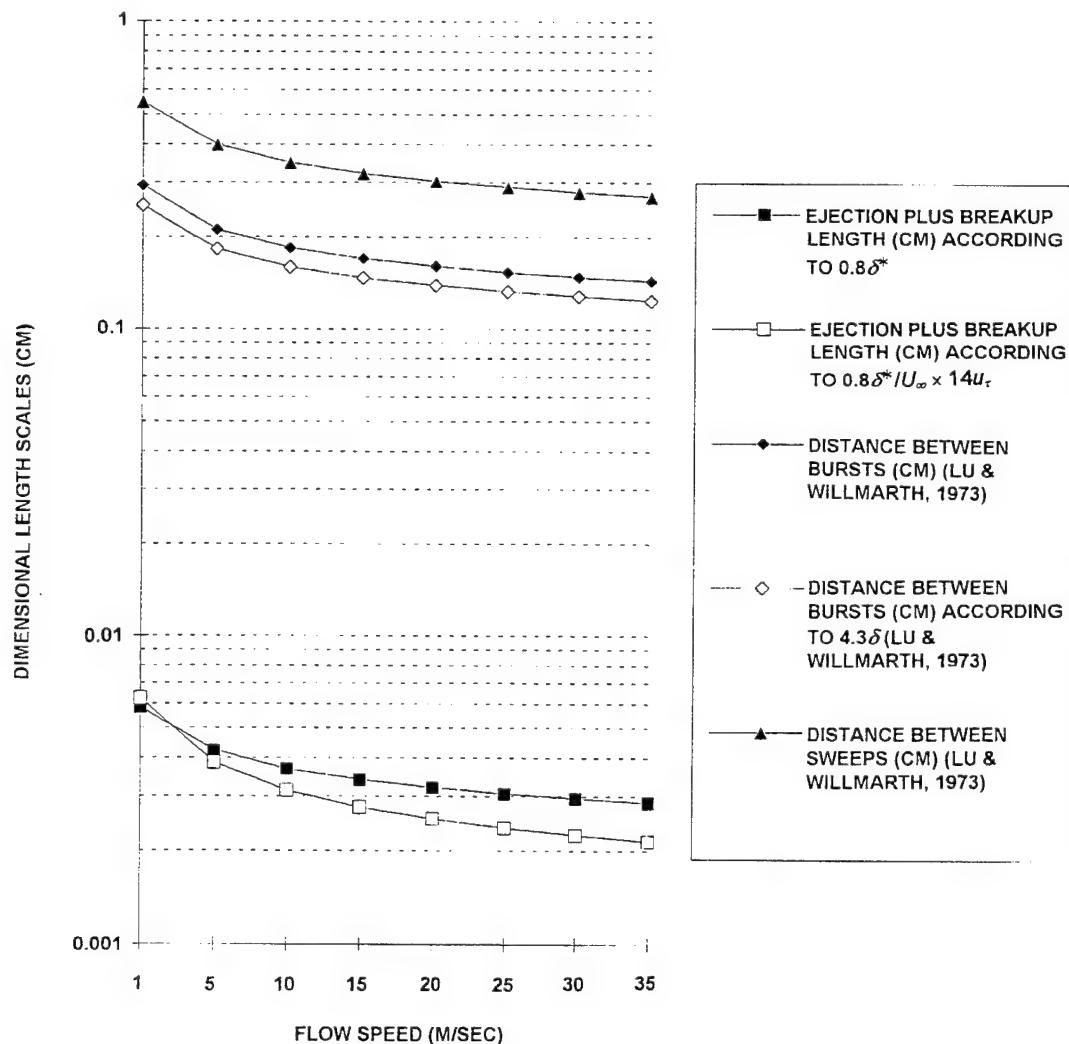
Figure 11. Dimensional Microturbulence Length Scales vs Flow Speed

22

3.2 DYNAMIC PARAMETERS

3.2.1 Natural Microturbulent Burst Power Scaling

It would be ideal if dynamic relationships could be derived for all microturbulent events. But, because of a dearth of frequency-per-span information for sweeps, only the power scaling for ejection-breakup events can be carried out, which is presented below. For practical applications of controlling turbulent drag, this might be sufficient, since the majority of Reynolds stress is produced during the burst period.

The power required for a microvortex ejection can be derived from basic dynamics principles. One starts with the definition of power:

$$\vec{F} \cdot \vec{u} = \frac{\Delta(m\vec{u})}{\Delta t} \cdot \vec{u} = \rho \frac{\Delta x \Delta y \Delta z}{\Delta t}(\Delta u + \Delta v) \cdot \vec{u}$$

$$= \rho \frac{(100)^2 \cdot 30}{20 \frac{v}{u_\tau^2}} \left(\frac{v}{u_\tau}\right)^3 \left[(14u_\tau^2) + u_\tau^2\right] \cong 2.1 \times 10^5 \rho u_\tau v^2,$$

where it is assumed that $\Delta x^+ = 100$, $\Delta y^+ = 30$, $\Delta z^+ = 100$, $\Delta t^+ = 20$, $\Delta u = u\ (y^+ = 60) - u\ (y^+ = 30) = u_\tau$, $\Delta v = u_\tau$, and the local velocity vector is assumed to be $u = 14u_\tau$, $v = u_\tau$. From this relationship, one can easily calculate the energy per ejection by multiplying the above expression of power per ejection by $20v/u_\tau^2$:

$$\cong 4.2 \times 10^6 \rho \frac{v^3}{u_\tau}.$$

The next step is to calculate the power per unit area in a natural burst cycle:

Power per unit area = energy/ejection × number of bursts/span/sec/burst separation

$$= 4.2 \times 10^6 \rho \frac{v^3}{u_\tau} 1.5 \times 10^{-4} \frac{u_\tau^3}{v^2} \frac{1}{T_B 14 u_\tau} = 69 Re_\theta^{-0.73} \rho u_\tau^3.$$

From these relationships, the natural microturbulent burst scaling for $5 \times 10^5 < Re_x < 10^7$ can be summarized:

Dynamics:
Vortex liftup force per ejection $\cong 2.1 \times 10^5 \rho v^2$
Vortex liftup power per ejection $\cong 2.1 \times 10^5 \rho u_\tau v^2$
Vortex liftup energy per ejection $\cong 4.2 \times 10^6 \rho v^3 / u_\tau$

Power:
Natural microejection power required per unit area $\cong 69 Re_\theta^{-0.73} \rho u_\tau^3$

It is, however, important to point out that bursting contributes significantly to Reynolds stress but accounts for only a small fraction of the dynamics, as would be expected. This fact can be demonstrated by comparing ejection power per unit area with $1/2 \rho U^3 c_f$ and examining the ratio, which can be expressed as $\approx 20 Re_\theta^{-0.855} \cong 0.05$ and $\cong 0.007$ for $Re_\theta \cong 10^3$ and 10^4, respectively.

3.2.2 Threshold Lorentz Pressure Power for Electromagnetic Turbulence Control (EMTC)

The threshold Lorentz pressure required for EMTC can be derived by comparing the Lorentz pressure power per unit area with the power per unit area in natural microturbulent burst cycles. Conceptually, the threshold is where this ratio equals one. Before one can proceed to derive this ratio, one must establish the length and time scale assumptions, which are summarized below:

Length Scales:
Spanwise spacing of Lorentz pressure	$100 v/u_\tau$
Distance normal to wall of Lorentz pressure	$30 v/u_\tau$

Time Scales (if pulsed or ac):
Lorentz pressure frequency	$1/T_B$
Lorentz pressure pulse duration	$20 v/u_\tau^2$

Since it is not clear *a priori* that this threshold would be identical to that for the case of Lorentz pressure in the streamwise flow direction or direction normal to the solid wall over which turbulence is generated, calculations will be carried out for both of these cases. For the normal Lorentz pressure, the Lorentz pressure power/area $= \Delta p \cdot \vec{u}$. Since the power required per unit area in natural burst cycles is $\cong 69 Re_\theta^{-0.73} \rho u_\tau^3$, the power per unit area in natural burst cycles in terms of length Reynolds number can be derived to be $\cong 781 Re_x^{-0.584} \rho u_\tau^3$. The threshold Lorentz power must then be equal to or greater than the power required in the natural cycle:

$$\Delta p \cdot \vec{u} = \int_0^{40\frac{v}{u_\tau}} \vec{J} \times \vec{B} \cdot \vec{u} \, dy$$

$$= J_0 B_0 \int_0^{40\frac{v}{u_\tau}} e^{-\frac{2y}{a}} \vec{e}_y \cdot \vec{u} \, dy$$

$$= -J_0 B_0 \int_0^{40\frac{v}{u_\tau}} e^{-\frac{2y}{a}} v \, dy.$$

where $\vec{J}$ and $\vec{B}$ are the externally applied electrical current density and magnetic flux density vectors, respectively.

In a turbulent boundary layer without an axial pressure gradient, the local vertical velocity has zero mean. The vertical velocity is away from the wall during ejection and bursting, and it is toward the wall during sweep. Unless the Lorentz pressure is sustained long enough to give rise

24

to a velocity along the Lorentz pressure gradient vector, no net work would be done to the flow. In practice, this implies that the EMTC pulse duration should be longer than the combined durations of ejection and bursting. Assuming that a velocity normal to the wall on the order of the natural turbulence, $v \cong u_\tau$ in the active MHD region, then

$$\Delta p \cdot \vec{u} = \frac{J_0 B_0 a u_\tau}{2}\left(1 - e^{-\frac{80v}{u_\tau}}\right),$$

which is a highly idealized candidate for an order-of-magnitude estimation. In other words, the magnetohydrodynamics (MHD) interaction parameter must satisfy

$$\frac{J_0 B_0 a}{1/2 \rho u_\tau^2}\left(1 - e^{-\frac{80v}{u_\tau a}}\right) \geq \frac{3124}{Re_x^{0.584}}.$$

For the streamwise Lorentz pressure gradient case, the local velocity is $u \cong 14\, u_\tau$:

$$\Delta p \cdot \vec{u} = \int_0^{40\frac{v}{u_\tau}} J_0 B_0 e^{-\frac{2y}{a}} u(y)dy, \qquad u(y) = u_\tau \frac{y u_\tau}{v} \text{ up to } 10\frac{v}{u_\tau} \text{ and beyond that}$$

$$u(y) = u_\tau\left(5.5\log y^+ + 5.2\right);$$

$$\Delta p \cdot \vec{u} = \int_0^{40\frac{v}{u_\tau}} J_0 B_0 e^{-\frac{2y}{a}} u_\tau \frac{y u_\tau}{v} dy + \int_{10\frac{v}{u_\tau}}^{40\frac{v}{u_\tau}} J_0 B_0 e^{-\frac{2y}{a}} u_\tau\left[5.5\log\left(\frac{y u_\tau}{v}\right) + 5.2\right]dy,$$

$$= J_0 B_0 u_\tau a \begin{bmatrix} \frac{u_\tau a}{4v}\left(1 - e^{-\frac{20v}{u_\tau a}}\right) - 5e^{-\frac{20v}{u_\tau a}} + 2.6\left(e^{-\frac{20v}{u_\tau a}} - e^{-\frac{40v}{u_\tau a}}\right) \\[2ex] + 2.75\log\left(\frac{u_\tau a}{2v}\right)\left(e^{-\frac{20v}{u_\tau a}} - e^{-\frac{80v}{u_\tau a}}\right) + \int_{\frac{20v}{u_\tau a}}^{\frac{80v}{u_\tau a}} e^{-\xi}\log\xi\, d\xi \end{bmatrix},$$

so that, since the power/area in the natural burst cycle $\cong 781 Re_x^{-0.584} \rho u_\tau^3$, the threshold Lorentz power would then follow:

$$\frac{J_0 B_0 a}{1/2 \rho u_\tau^2}\{\cdot\} \geq \frac{1562}{Re_x^{0.584}},$$

where $\{\cdot\}$ represents the long expression of the geometric factor in terms of the EMTC cell spacing parameter $u_\tau a/v$. It is interesting to note that the threshold Lorentz pressure, in terms of the MHD interaction parameter, is higher for the Lorentz pressure gradient normal to the wall than for the streamwise case along the flow.

One way to illustrate this threshold condition is by displaying the ratio of the left-hand side and the right-hand side as a function of the MHD interaction parameter $JBa/\rho u_\tau^2$, and the spacing Reynolds number $u_\tau a/v$ as a function of the length Reynolds number. When this ratio is close to or greater than 1, the turbulence control is expected to be effective; a ratio below 1 implies less effectiveness, and a ratio much above 1 may mean overexertion of control, implying less efficiency. Figure 12 presents the case of free-stream Reynolds number $= 10^5$.
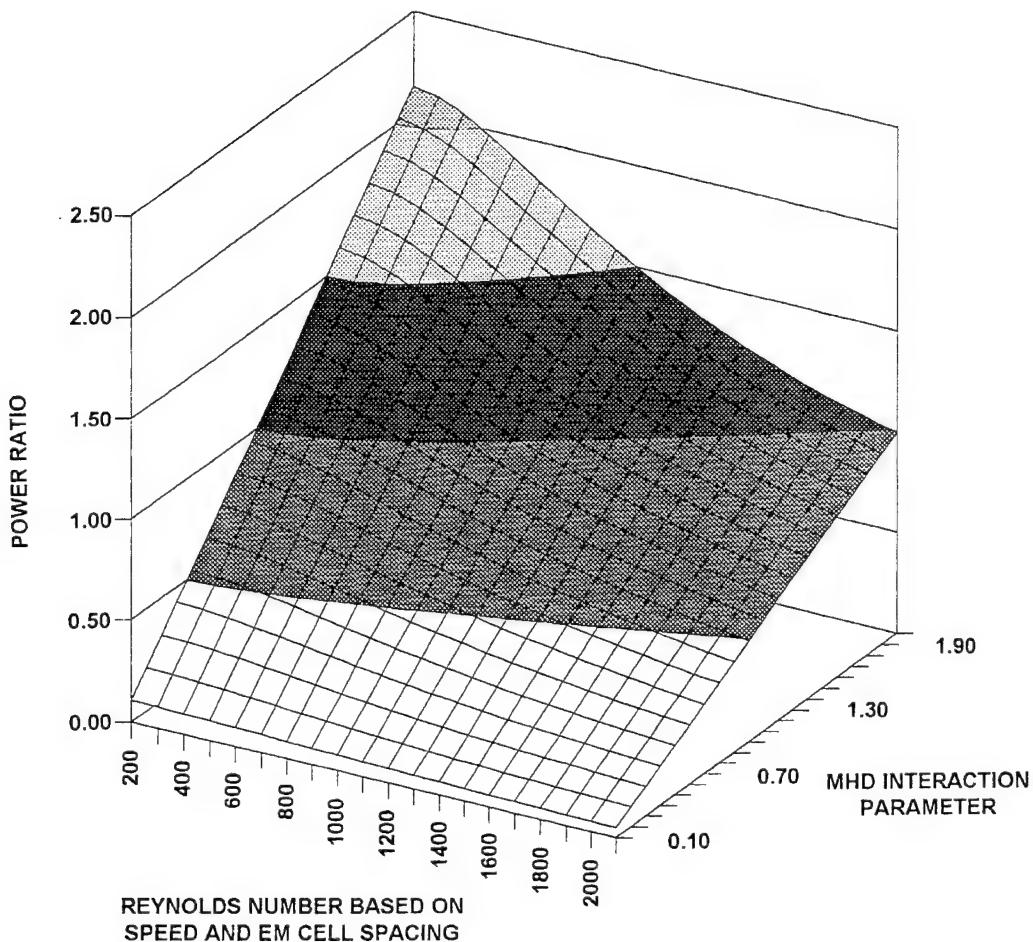
Figure 12. Ratio of Lorentz Power for EM Control of Microturbulence to Natural Microturbulent Burst Power vs MHD Interaction Parameter and EMTC Cell Spacing Reynolds Number at Free-Stream Reynolds Number of 10^5

26

Similarly, figure 13 shows the case where Reynolds number = 10^7 over the same domain of cell spacing Reynolds number and MHD interaction parameter as in figure 12. By comparing the two graphs, one can see that as the free-stream Reynolds number increases, the ratio increases for the same cell spacing Reynolds number and MHD interaction parameter.

It is interesting to note that the ratio is the highest for small spacing of electrodes and magnets and an MHD interaction parameter value greater than 1. The ratio decreases as spacing increases and the MHD interaction parameter decreases. Both trends are consistent with a rudimentary understanding of electromagnetic control of turbulence in a conducting medium. It is also interesting that, as the free-stream Reynolds number increases, the ratio increases, implying that for the same EM cells and MHD interaction parameter the turbulence control effectiveness increases. By setting the ratio to be unity, one can relate the EM cell spacing to the MHD interaction parameter as a function of free-stream Reynolds number, thereby defining the
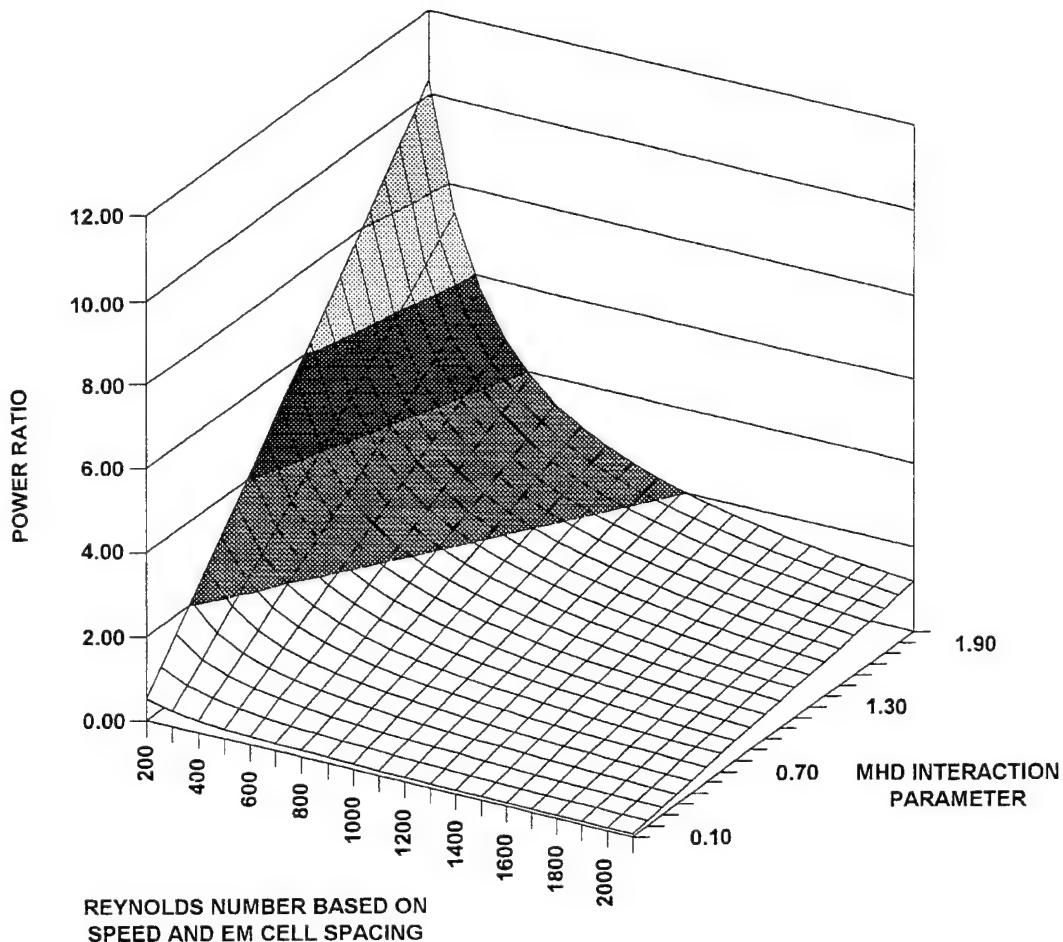

Figure 13. Ratio of Lorentz Power for EM Control of Microturbulence to Natural Microturbulent Burst Power vs MHD Interaction Parameter and EMTC Cell Spacing Reynolds Number at Free-Stream Reynolds Number of 10^7

27

threshold condition as a function of Reynolds number. Specifically, this can be expressed as

$$Re_a = -415.9Re_x^{0.1}/\ln(1 - 781N_{im}Re_x^{0.584}).$$

This expression is illustrated in figure 14.
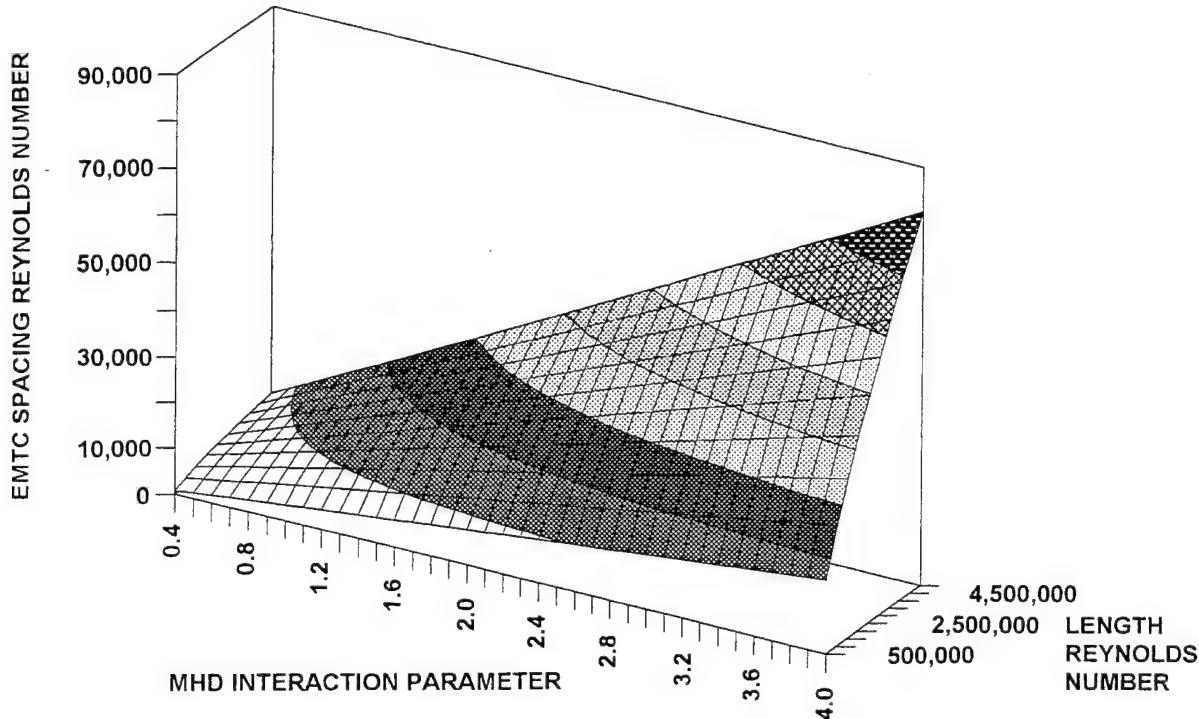
Figure 14. EMTC Spacing Reynolds Number as a Function of MHD Interaction Parameter and Length Reynolds Number at Threshold Condition

3.2.3 EMTC Efficiency

To obtain an indicator of the effectiveness of any EMTC approaches (normal or axial or any other configuration), the efficiency concept is introduced. One seeks an analytic expression that will relate some basic design parameters expressed in terms of nondimensional parameters to the flow's nondimensional parameters, such as the Reynolds number, MHD interaction parameter, load factor, and electrode parasitic voltage losses. This expression can be used to guide the point design as more practical approaches are introduced. First, the ideal efficiency is defined as

$$\eta_i = \frac{\text{Power Saved by EMTC}}{\text{Input Power to Electrodes}}.$$

28

The power saved by EMTC per unit area $= 1/2\rho U^3 \Delta c_f$, where c_f is the friction coefficient, and the power input to the electrodes per unit area $= IV$, where I is the electrical current and V is the voltage, so that

$$\eta_i = \frac{\frac{1}{2}\rho U^3 \Delta c_f}{IV}.$$

This ratio can be decomposed into products of efficiencies of several dominant physical processes; namely,

η_i = (pwr saved by EMTC per unit area / pwr expended due to natural turbulence production per unit area)

* (pwr expended due to natural turbulence production per unit area / Lorentz pressure pwr per unit area)

* (Lorentz pressure pwr per unit area / electrical pwr delivered in seawater per unit area)

* (electrical pwr delivered in seawater per unit area / input electrode pwr per unit area).

In other words, the above expression can be interpreted as the product of several intermediate efficiencies:

η_i = (turbulent drag reduction efficiency) * (drag / Lorentz power ratio)

* (electromagnetohydrodynamic efficiency) * (seawater electrode efficiency).

Specifically, η can be expressed as the product of the following ratios:

$$\frac{\text{Turbulent Drag Reduction}}{\text{Natural Turbulent Drag}} * \frac{\text{Natural Turbulent Drag}}{\text{Lorentz Pressure Power}} * \frac{\text{Lorentz Pressure Power}}{\text{Electrical Power in Water}} * \frac{\text{Electrical Power in Water}}{\text{Input Electrode Power}}$$

$$\eta = \frac{\Delta c_f}{c_f} \quad \bullet \quad \frac{\frac{1}{2}\rho U^3 c_f}{J_0 B_0 a\left(1-e^{\frac{-80v}{u_\tau a}}\right)10u_\tau} \bullet \frac{J_0 B_0 a\left(1-e^{\frac{-80v}{u_\tau a}}\right)10u_\tau}{I(V-V_0)} \bullet \frac{I(V-V_0)}{IV} = \frac{\frac{1}{2}\rho U^3 \Delta c_f}{IV}$$

$$= \frac{\Delta c_f}{c_f} \quad \bullet \quad \frac{\rho u_\tau^2}{J_0 B_0 a}\sqrt{\frac{2}{100 c_f}} \quad \bullet \quad \frac{10 u_\tau B}{E\left(1-\frac{V_0}{V}\right)} \quad \bullet \quad \left(1-\frac{V_0}{V}\right)$$

$$= \frac{\Delta c_f}{c_f} \quad \bullet \quad \sqrt{\frac{2}{c_f}} \quad \bullet \quad \frac{\rho u_\tau^2}{J_0 B_0 a} \quad \bullet \quad \frac{u_\tau B}{E}.$$

It is interesting to note that the major physical dimensionless parameters — imposed MHD interaction parameter $N_{im} \equiv (J_0 B_0 a)/\rho u_\tau^2$, electrical load factor $L \equiv E/(u_\tau B)$, and potential ratio V/V_0 — emerge in these expressions. The same results can be obtained by a rigorous application of the pi-theorem.

Examining these expressions, one can see that

$$\eta_i \propto \frac{\Delta c_f}{c_f} \frac{1}{N_{im}} \sqrt{\frac{2}{c_f}} \cdot \frac{1}{L},$$

so that as $N_{im} \to 0$ and $L \to 0$, η_i would approach infinity. This simplistic argument neglects the fact that as $N_{im}, L \to 0$, meaning that no EMTC is applied, $\Delta c_f/c_f \to 0$; therefore, $\eta \to 0$. The interesting behavior of $\eta_i \to 0$ as $N_{im}, L \to 0$ must await more detailed experimental observation or asymptotic theoretical analysis of small N_{im} and L parameters.

Another point concerns the ratio V_0/V, where V_0 is the electrode's overpotential. To deliver electrical power into seawater, V_0/V must be less than 1. As V_0/V decreases, the electrical efficiency decreases linearly. For practical applications, the ratio V_0/V ranges from 0.1 to 0.5. The smaller value of V_0/V herein implies larger N_{im} and L. Therefore, to increase η_i, one must optimize the entire system, not just the individual terms. Note also that $\Delta c_f/c_f$ is a function of N_{im}, c_f, and L. Since c_f is a function of Re_θ, $\Delta c_f/c_f$ is a function of Re_θ, N_{im}, and L, and can be obtained only via systematic experimental measurements. The dependence of $\Delta c_f/c_f$ on N_{im} and L must be consistent with its behavior near the origin of the N_{im}, L, Re_θ coordinates. In other words, $\Delta c_f/c_f$ should be

$$\frac{\Delta c_f}{c_f} = N_{im}^{1+a} L^{1+b} f(Re_\theta, N_{im}, L),$$

so that $\eta_i = N_{im}^a L^b f(Re_\theta, N_{im}, L)$, where a and b are any positive values. To satisfy the large N_{im}, L value limit behaviors, i.e., $\partial \eta_i/\partial N_{im} < 0$ with $N_{im} \gg 0$, $L \gg 0$, one expects that $\partial \ln f/\partial \ln N_{im} < a$ and $\partial \ln f/\partial \ln L < b$. These conditions can guide experimenters in analyzing measurement data. Based on experience with seawater MHD propulsion tests and the above observations, one can conjecture η_i to be of the following form:

$$\eta_i \propto N_{im}^a L^b e^{-N_{im}} e^{-L},$$

which has a single peak at $(N_{im}, L) = (a, b)$.

4. MARKOV TRANSITION PROBABILITY AS A DIAGNOSTIC TOOL FOR CHARACTERIZING AND CONTROLLING WALL MICROTURBULENT EVENTS

4.1 HYPOTHESIZED MARKOV CHAIN OF MICROTURBULENT EVENTS

The wall layer microturbulent events are mutually dependent and can be related to the Markov chain of stochastic processes, which is depicted in figure 15.
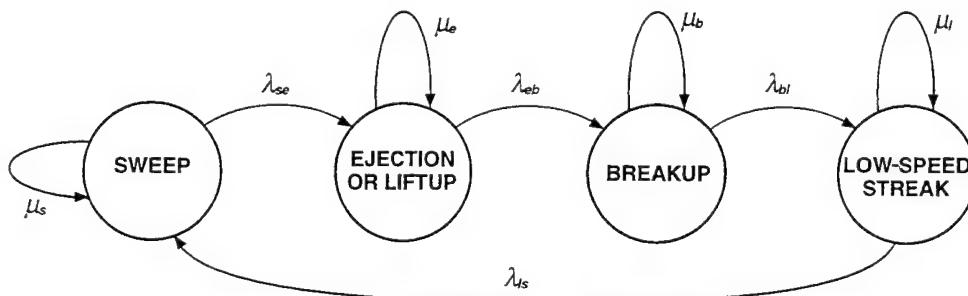

Figure 15. Markov Chain of Stochastic Processes

Note the similarity of this chain to the continuous birth-and-death chain well known in Markov analysis. It is a single-chain, quasi-continuous process. As shown in figure 15, the assumptions are that the entire event chain is characterized by the few identifiable discrete events, and the reverse transition probabilities from any state to the previous state are zero, except for the eventual low-speed streak state to sweep state. The transition probabilities are λ_{ij}'s, and the distinctive states are characterized by the percentage of time resident in each state. One certainly can argue that not all low-speed streaks lead to liftup; although if the local Reynolds number exceeds the transition limit, it is certain that eventual transition will occur to the hairpin vortex liftup, which ultimately leads to the breakup state. One should further note that the turbulent events form a single-chain, quasi-continuous birth-and-death process. This assertion is based on the observation that no periodic states exist. It is important not to confuse Markov periodic states with the periodically occurring discrete states in a turbulent boundary layer. The former exist if, for every k-number of experimental trials, a particular state emerges, which is certainly not the case in the wall layer microturbulent events. The latter are states that occur with predicable periodicity over certain spatial and temporal scales.

Several issues regarding the Markov representation of the discrete events in a turbulent boundary layer remain to be addressed. Among these are the satisfaction of the Markov process definition, i.e., that there is only a finite number of discrete states, the probability of any state depends only on the probability of the previous state in the time sequence, the existence of limiting states, and their corresponding limiting probabilities. Resolution of these issues must await later theoretical analyses.

4.2 MARKOV TRANSITION PROBABILITIES IN
THE ABSENCE OF EXTERNAL FORCES

The four microturbulent states are mutually dependent and they occur according to a specific sequence. To describe the probabilistic model, one starts from the Chapman-Kolmogorov equation $p_i'(t) = -\mu_i p_i + \Sigma \lambda_{ji} p_j(t)$, where ' represents the time derivative. This equation states that the rate of change of probability of any one state is determined by the regeneration rate of itself and the transition probabilities of other states multiplied by the probabilities of that state. Stated in terms of the four mutually exclusive microturbulent states—l for low-speed streak, e for ejection, b for breakup, and s for high-speed sweep, one can rewrite the above equation as follows:

$$p_e'(t) = -\mu_e p_e(t) + \Sigma \lambda_{je} p_j(t),$$
$$p_b'(t) = -\mu_b p_b(t) + \Sigma \lambda_{jb} p_j(t),$$
$$p_s'(t) = -\mu_s p_s(t) + \Sigma \lambda_{js} p_j(t), \text{ where } \Sigma \text{ is over all } j\text{'s,}$$
$$p_l(t) + p_e(t) + p_b(t) + p_s(t) = 1.$$

If one assumes that the microturbulent states follow a continuously cyclic process, in other words the transition probabilities are nonzero only for those states in the observed sequence, i.e., $\lambda_{el} = \lambda_{es} = \lambda_{be} = \lambda_{bs} = \lambda_{sb} = \lambda_{be} = \lambda_{sl} = \lambda_{lb} = 0$, then the above equations become:

$$p_e'(t) = -\mu_e p_e(t) + \lambda_{se} p_s(t),$$
$$p_b'(t) = -\mu_b p_b(t) + \lambda_{eb} p_e(t),$$
$$p_s'(t) = -\mu_s p_s(t) + \lambda_{ls} p_l(t),$$
$$p_l(t) + p_e(t) + p_b(t) + p_s(t) = 1.$$

These equations can be solved analytically if all λ_{ij}'s and μ's are constants.

4.3 MARKOV LIMITING PROBABILITIES FOR
NATURAL TURBULENT BOUNDARY LAYERS

All of the experimental measurements reported are based on long-duration averages that show the sequence of near-wall events: liftup and ejection, breakup, low-speed streak, and high-speed sweep toward the wall. The entire cycle then repeats itself. These states are mutually exclusive and exhaustively collective to describe any possible state of the turbulent boundary layer. Probabilistic analysis of results of any point diagnosis of local state in a turbulent boundary layer must, however, consider transition probabilities from all neighboring streaks and ensuing structures. This implies that even though the instantaneous point observations in a Eulerian frame of reference show random migration of neighboring streaks' sequence of discrete events, such as the sequence of streak-to-vortex liftup then back to streak from a neighboring streak, the long-duration observation (i.e., over a time scale of $t \gg$ period of the breakup or burst cycle) shows

only the above four discrete events, which occur periodically and indefinitely, until flow conditions change. Therefore, probabilistically speaking, it suffices to say that after many statistical trials, i.e., as the number of observations approaches infinity, limiting probabilities (P_i's) exist for each discrete event. In principle, one could then use the Chapman-Kolmogorov equation to derive the limiting state probabilities, provided that detailed measurement data exist over a very short time scale (a time scale shorter than a small fraction of the burst period) and provided that a reliable signal processing algorithm is available to record and detect all transition probabilities from neighboring states. This derivation would be very technically demanding and time-consuming.

In the case of fully developed turbulent flows without externally applied unsteady forces, one expects that the stochastic process will asymptote to the limiting states, i.e., the time derivatives vanish, so that a stationary stochastic process can be established. This is mathematically possible if the regeneration rates and transition probabilities follow the known sequence and, therefore, the following conditions:

$$\mu_e = \lambda_{eb},$$
$$\mu_b = \lambda_{bl},$$
$$\mu_s = \lambda_{se},$$
$$\mu_l = \lambda_{ls}.$$

With some rearrangement and substitution, the following solutions can be established in terms of the arrival rates μ's:

$$p_s = 1/\left(1 + \frac{\mu_s}{\mu_e} + \frac{\mu_s}{\mu_l} + \frac{\mu_s}{\mu_b}\right),$$

$$p_e = \frac{\mu_s}{\mu_e} p_s,$$

$$p_l = \frac{\mu_s}{\mu_l} p_s,$$

$$p_b = \frac{\mu_s}{\mu_b} p_s.$$

These rates can be determined experimentally from the mean time between arrivals. For practical applications, the arrival rates for ejection, breakup, and sweep can be assumed to be the same as the experimentally measured burst rate. The arrival rate for the low-speed streaks can be estimated by multiplying the burst rate by the ratio of streak coherence length to ejection and burst length (≈ 12), or by the ratio of burst period to combined individual ejection-breakup-sweep duration (≈ 30).

In summary, the measurement data, by definition, have already provided the information, based on the limiting states, that can help to determine the limiting probabilities. Specifically,

one can use the experimentally observed mean time between occurrence of events to determine the birth rates of each event, and then apply the Chapman-Kolmogorov equation to calculate the limiting probabilities. Once the probabilities are determined, many statistical parameters can be obtained to aid practical implementation of EMTC. To illustrate the methodology, one can simplify the real-time calculation by assuming that the ejection and breakup states can be combined. This assumption then yields the following equations governing the limiting states condition, i.e., all derivatives vanish:

$$p_s = \frac{1}{\left(1 + \dfrac{\mu_s}{\mu_e} + \dfrac{\mu_s}{\mu_l}\right)},$$

$$p_e = \frac{\mu_s}{\mu_e} p_s,$$

$$p_l = \frac{\mu_s}{\mu_l} p_s.$$

With this approach, only the arrival rates of the ejection/breakup and sweep states need to be measured from the experimental data.

4.4 MARKOV TRANSITION PROBABILITIES WITH EMTC APPLIED

In a natural turbulent boundary, the sequential order described in the phenomenological cycle is the only allowable mode of transition. Since all transition must occur with eventual certainty, one finds that the limiting states apply. Given that the frequency of occurrence of each state is proportional to the probability of each state, the experimentally obtained fractional times of ejection, breakup, sweep, and low-speed streaks serve as a guide to demark the wall pressure fluctuation and wall shear stress histograms into four nonoverlapping regimes. The transition probabilities λ_{ij}'s are related to the experimentally measured arrival rates.

When an external influence is activated, the transition probabilities no longer are certain and the sequential order may not be preserved; in fact, some reverse transition is conceivable, although the natural tendencies must still be overwhelming. In this case, the full set of transition probabilities must be dealt with. For the unsteady case, the full set of state probability equations is as follows:

$$p_e'(t) = -\mu_e p_e(t) + \mu_s p_s(t),$$
$$p_b'(t) = -\mu_b p_b(t) + \mu_e p_e(t),$$
$$p_s'(t) = -\mu_s p_s(t) + \mu_l p_l(t),$$
$$p_e(t) + p_b(t) + p_l(t) + p_s(t) = 1.$$

34

To solve this set of equations, one must make some assumptions about the arrival rates. First, one assumes that the arrival rates are independent of time, as the experimental data indicate for the natural turbulent boundary layer. The question then becomes: Does this assumption apply to the case where externally applied forces are present? Second, one assumes that the time-varying state probability depends on how much control is to be imposed. These assumptions are connected and are solely a function of the control methodology. If the control methodology is to completely eliminate turbulence, i.e., totally eliminate the microturbulent events, then the arrival rates would be zero, and the states representing each microturbulent event would not exist, and the local flow would surely correspond to laminar flow conditions. Knowing that the microturbulent events represent the most stable flow configurations under turbulent conditions that nature can provide, the control methodology should be one that is in harmony with nature rather than one that tries to overcome nature. Therefore, the turbulence control methodology adopted here is to mitigate or minimize the occurrence of microturbulent events. Given that the control methodology is based on inhibiting turbulence rather than on totally eliminating it, the rate of change of state probabilities should be small compared with the limiting state probabilities, i.e.,

$$\tilde{T}_B \frac{d}{dt}\ln p_e(dt), \ \tilde{T}_B \frac{d}{dt}\ln p_b(dt), \ \text{and} \ \tilde{T}_B \frac{d}{dt}\ln p_s(dt) \ \text{all should be much smaller than 1. Then, the}$$

first assumption (viz., that the arrival rates are not different from in the natural state) is satisfied, and the second assumption is addressed by using only marginal control to maintain the turbulent state at a much lower level of turbulence production.

Given the above assumptions, the differential equations can be solved versus time. To illustrate the process, the above equations can be simplified by assuming that ejection is followed by breakup, so that only three states need to be considered, i.e.,

$$p_e'(t) = -\mu_e p_e(t) + \mu_s p_s(t),$$
$$p_s'(t) = -\mu_s p_s(t) + \mu_l\big[1 - p_e(t) - p_s(t)\big],$$

with the initial conditions $p_e(0)$, $p_s(0)$, $p_l(0)$ equal to the limiting state probabilities in natural turbulent boundary layers. The above equations can be represented by

$$\frac{d}{dt}\begin{bmatrix} p_e(t) \\ p_s(t) \end{bmatrix} = \big[p_e(t), p_s(t)\big]\begin{bmatrix} -\mu_e & -\mu_l \\ \mu_s & -\mu_l + \mu_s \end{bmatrix} + \begin{bmatrix} 0 \\ \mu_l \end{bmatrix}.$$

This equation has the exponential solution $e^{\alpha t}$, where the α's are eigen-values of the coefficient matrix

$$\begin{bmatrix} -\mu_e & \mu_s \\ -\mu_l & -(\mu_l + \mu_s) \end{bmatrix}.$$

The two α_1, α_2 are roots of the following quadratic equation:

$$(\alpha + \mu_e)(\alpha + \mu_l + \mu_s) + \mu_l\mu_s = 0.$$

35

If one substitutes the following into the state probability differential equations,

$$\begin{bmatrix} p_e(t) \\ p_s(t) \end{bmatrix} = \begin{bmatrix} p_{en}(t) \\ p_{sn}(t) \end{bmatrix} e^{\alpha t},$$

where p_{en} and p_{sn} are the nonhomogeneous parts of ordinary differential equations, one obtains

$$\frac{d}{dt} \begin{bmatrix} p_{en}(t) \\ p_{sn}(t) \end{bmatrix} = \begin{bmatrix} 0 \\ \mu_l \end{bmatrix} e^{-\alpha t},$$

which can be solved easily as

$$\begin{bmatrix} p_{en}(t) \\ p_{sn}(t) \end{bmatrix} = \begin{bmatrix} C \\ \dfrac{\mu_l}{\alpha}(1-e^{-\alpha t})+D \end{bmatrix},$$

or

$$\begin{bmatrix} p_e(t) \\ p_s(t) \end{bmatrix} = \sum_i^{1,2} \begin{bmatrix} C_i e^{\alpha_i t} \\ \dfrac{\mu_l}{\alpha_i}(e^{\alpha_i t}-1)+D_i e^{\alpha_i t} \end{bmatrix}.$$

The total solution is then

$$p_e(t) = 0.5 \cdot p_e(o)\left[e^{\alpha_1 t} + e^{\alpha_2 t}\right],$$

$$p_s(t) = 0.5 \cdot p_s(o)\left[e^{\alpha_1 t} + e^{\alpha_2 t}\right] + \left[\frac{\mu_l}{\alpha_1}(e^{\alpha_1 t}-1) + \frac{\mu_l}{\alpha_2}(e^{\alpha_2 t}-1)\right].$$

Note that α_1, α_2 are complex conjugates; p_e and p_s are always real numbers, which is consistent with the probability concept.

The consistency of these solutions can best be demonstrated by a simple example of numerical results. First of all, the values of the arrival rates μ_l, μ_e, and μ_s need to be determined from the experimental data. Using the time durations listed in table 2 for ejection, breakup and sweep, the μ's can be evaluated to be $\mu_l \approx 31.5/32$, $\mu_e \approx 0.2/32$, and $\mu_s \approx 0.3/32$. The two α's can be found to be $\alpha_1 \approx 0.015 + 0.124i$ and $\alpha_2 \approx 0.015 - 0.124i$. From these values, the probabilities of states e, s, and l can be calculated as a function of time. For a hypothetical case where $\mu_l = 0.37$, $\mu_e = 0.68$, and $\mu_s = 0.68$, the two roots are -0.87 + 0.47i and -0.87 - 0.47i. Figure 16 shows the crossover from low-speed streak to sweep.
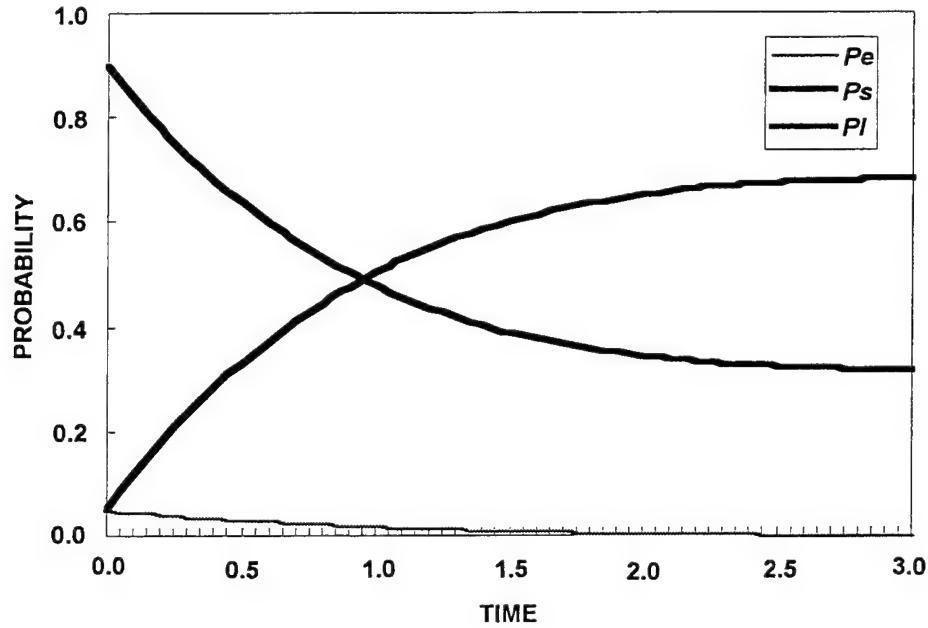
***Figure 16. Sample Calculated Results for Discrete Micoturbulent Markov State
Probability vs Time, Illustrating Crossover from Low-Speed Streak to Sweep***

Similarly, the full set of p_s, p_e, p_b, p_l equations can be solved; the analytic solutions are derived below:

$$\frac{d}{dt}\begin{bmatrix} p_s \\ p_e \\ p_b \end{bmatrix} = \begin{bmatrix} -(\mu_s + \mu_l) & -\mu_l & -\mu_l \\ \mu_s - \mu_e & -\mu_e & 0 \\ 0 & \mu_e & -\mu_b \end{bmatrix}\begin{bmatrix} p_s \\ p_e \\ p_b \end{bmatrix} + \begin{bmatrix} \mu_l \\ 0 \\ 0 \end{bmatrix}.$$

The exponent α's are eigenvalues of the matrix

$$\begin{bmatrix} -(\mu_s + \mu_l) & -\mu_l & -\mu_l \\ \mu_s & -\mu_e & 0 \\ 0 & \mu_e & -\mu_b \end{bmatrix},$$

i.e.,

$$(\alpha + \mu_s + \mu_l)(\alpha + \mu_e)(\alpha + \mu_b) + (\alpha + \mu_b)\mu_s\mu_l + \mu_s\mu_e\mu_l = 0,$$

or

$$\alpha^3 + \alpha^2(\mu_s + \mu_e + \mu_b + \mu_l) + \alpha(\mu_s\mu_e + \mu_s\mu_b + \mu_e\mu_b + \mu_b\mu_l + \mu_l\mu_e + \mu_s\mu_l)$$
$$+ \mu_e\mu_b(\mu_s + \mu_l) + \mu_l\mu_s(\mu_e + \mu_b) = 0.$$

37

Then,

$$
\begin{bmatrix} p_s \\ p_e \\ p_b \end{bmatrix} = \begin{bmatrix} p_{sn} \\ p_{en} \\ p_{bn} \end{bmatrix} e^{\alpha t}, \quad \text{and} \quad \frac{d}{dt} \begin{bmatrix} p_{sn} \\ p_{en} \\ p_{bn} \end{bmatrix} = \begin{bmatrix} \mu_l \\ 0 \\ 0 \end{bmatrix} e^{-\alpha t},
$$

so that

$$
-\begin{bmatrix} p_s(t) \\ p_e(t) \\ p_b(t) \end{bmatrix} = \begin{bmatrix} Ce^{\alpha t} + \dfrac{u_l}{\alpha}(e^{\alpha t} - 1) \\ De^{\alpha t} \\ Ee^{\alpha t} \end{bmatrix},
$$

in the same manner as the simplified case shown before.

There are two noteworthy points to make regarding these solutions. First, since all μ values are positive and less than 1, the eigenvalues are summed to be equal to $\mu_s + \mu_e + \mu_b + \mu_l \equiv 1$. Second, the product of all three roots is positive and less than 1, implying that two are complex conjugate. The real root is positive and less than 1.

4.5 ESTIMATION OF MARKOV TRANSITION PROBABILITIES WITH EXTERNAL FORCES APPLIED

Two familiar ways of presenting turbulent boundary layer data are the wall shear stress and the wall pressure probability histograms; both can be conceptually useful indicators for purposes of microturbulent event control. It is well-known that shear stress is dominated by small-scale eddies near the wall, while the wall pressure power density results from both large eddies away from the wall and small eddies near the wall. So, in a global sense, the wall shear stress fluctuations exist primarily as a consequence of the inner wall events, while the wall pressure fluctuations are due to both inner and outer wall events. The low end of the wall shear stress histogram represents the vortex liftup and ejection and breakup part of the cycle, while the high end of the histogram indicates the sweep part of the cycle. Similarly, the wall pressure histogram provides another cross-examination of the local microturbulent events, where the shear stress and wall pressure probes are located.

Two fundamental issues need to be addressed. First, it is important to differentiate between the turbulence phenomenology in a moving framework of a single cycle and the wall shear stress or pressure measured on a stationary framework simultaneously receiving inputs from many phenomenological cycles. If one accepts that Taylor's hypothesis is applicable, then the problem can be simplified. One can integrate the area under the histogram to find the percentage of time each event occupies in the complete cycle, and then one can carry out calculations of Markov

transition probabilities via established stochastic theories. Second, however, to formulate a complete diagnostic and predictive tool of turbulence modification methodology, one must connect the mass, momentum, energy, or power density balance to the modification approaches. For the electromagnetic Lorentz pressure gradient approach, the mass is always conserved and unaffected by the control methodology. To account for momentum would require solving the Navier-Stokes equation, a nearly impossible undertaking at the present time. The power density balance in a global sense is possible for purposes of the experimental data trend analysis. This approach is presented as follows.

The spectra of both the shear stress and wall pressure provide different views of the effects of the same microturbulent events. The low wavenumber part of the wall pressure spectrum characterizes the power density content of outer layer events, as does the high wavenumber end for near-wall inner layer events. The same holds true for the wall shear stress spectrum. Although there are many competing arguments for explaining the low wavenumber end of the wall pressure spectrum, and although the high frequency and wavenumber end of the spectrum is controlled by the sensing frequency response, the objectives here deal only with the power density integrated under the spectrum, which is less sensitive to the details of the spectrum fine structure. For the shear stress frequency spectrum, the same caveat is applicable.

The challenge then is in how the transition probabilities are determined. One hypothesis is that the transition probabilities should be influenced by the power density ratio of the microturbulent event of the natural state to the sum of the power densities delivered by the Lorentz pressure gradients L_{ij} and the natural state P_{ij}. In the absence of an externally applied power density, the ratios are identically equal to 1. For regions where the Lorentz power density inhibits liftup, the ratio would be diminished by the Lorentz pressure gradient, and the transition probability λ_{se} is therefore correspondingly reduced from its natural transition value. For the axial Lorentz pressure gradient, the liftup process is stretched over longer time and spatial scales, and the transition probability is modulated by the ratio of power density of the liftup natural state to the sum of it and the axial Lorentz power density input. If the latter overwhelms, the transition probability from liftup to breakup is diminished. The transition probability equations are then:

$\lambda_{EMTCij} = \lambda_{ij}$ *in natural TBL* $\cdot P_{ij}/(P_{ij} + L_{ij})$, for all i's and j's,

where the P_{ij}'s and p_{ij}'s are transition power densities corresponding to those from the natural and controlled state i to state j, respectively. Altogether, there are 16 equations for 16 unknowns. Again, as in the phenomenological model, the derivation here is based entirely on the microturbulent events empirically revealed and known today. As more detailed information is obtained, the models can be refined accordingly. But the concept and basic process are the focus here rather than the details, which can be debatable in several cases. Certain discrete state transition probabilities can be determined purely theoretically; for others, one has to rely on the integrated power density under each state and relate the power density differences to the transition probabilities.

The methodology for estimating the current state of the turbulent boundary layer in the presence of applied external forces is now described, again using EMTC as an example. The

PDFs of wall shear stress and wall pressure fluctuation are shown in figures 17 and 18. They are as shown earlier (in figures 6 and 7) except that the PDFs are demarcated into several nonoverlapping regions. The first region is for the low-speed streaks, which generate the lowest level of shear stress fluctuation, so that this region occupies the zero-mean-value band of the shear stress PDF. Then comes ejection, which because of its induced counterflow has a local shear stress fluctuation that is above that of the no-ejection state but below the mean shear stress and, therefore, is at the negative end of the τ'_w value. For the breakup state, there is little or no specific measurement data describing how it affects the local shear stress fluctuation. Intuitively, however, one would expect that the shear stress fluctuation would be higher than the mean during breakup, so that it occupies the third region, just to the right of the mean shear stress value. During the sweep state, experimental evidence indicates increased shear stress fluctuation because high-momentum fluid from the logarithmic region is imparted toward the wall; therefore, the sweep state is at the high end of the shear stress PDF. With this relative ranking given, and with knowledge of the limiting probability of each state in a naturally occurring turbulent boundary layer (which equates to the areas under each region), one can then demarcate the PDF into nonoverlapping regions. The nonoverlapping comes from the fact that the four discrete states are mutually exclusive and exhaustively collective to describe the entire microturbulent cycle.

Similarly, one can estimate the amount of pressure fluctuation power contained in ejection, sweep, and overall burst by examining the wall pressure spectrum expressed in terms of inner variable dimensions. Figure 19 shows such an example. The wall pressure spectra were obtained by Blake (1970) and Schewe (1983) both in terms of wall units, but Schewe's spectral levels were normalized by the spectral level at zero frequency and had to be adjusted for comparison. As can be seen, the two data sets agree. From the microturbulence phenomenology discussed earlier, the mean burst frequency $\omega^+ \approx 0.06$, and for the burst event frequencies measured by Schewe (1983) $\omega^+ \approx 0.52$. These two frequencies demarcate the relative ranges of the wall events from events occurring away from the wall, so that the power contained in each category of events can be estimated by integrating over relevant ranges as is indicated in the figure.

4.6 SUMMARY OF MARKOV TRANSITION PROBABILITY METHODOLOGY

As applied to characterizing and controlling wall layer turbulence, the methodology of the Markov transition probability comprises two major steps—estimating and predicting. The estimator step involves the following. At time 0 before the active control is turned on, the flow characteristics are measured in real time by flush-mounted hot-film probes and hydrophones. The wall shear stress and wall pressure fluctuation PDF histograms and spectra are generated by data processing. The histograms of the key parameters, such as the time between bursts and the mean and variance of wall shear stress and wall pressure fluctuation are determined, from which the dimensionless parameters are calculated. Then, the established wall turbulence phenomenology models are applied to estimate the mean time between bursts, burst duration, and spacing. The fractional time duration of each event as normalized by the average mean time between burst arrivals T_B is determined. The arrival rate or frequency of each microturbulent event is estimated from the fractional time duration. The limiting state probabilities are then determined from the arrival rate, as was derived in a previous section. These limiting state probabilities are stored. After several T_B periods, the limiting state probabilities are averaged and stored.
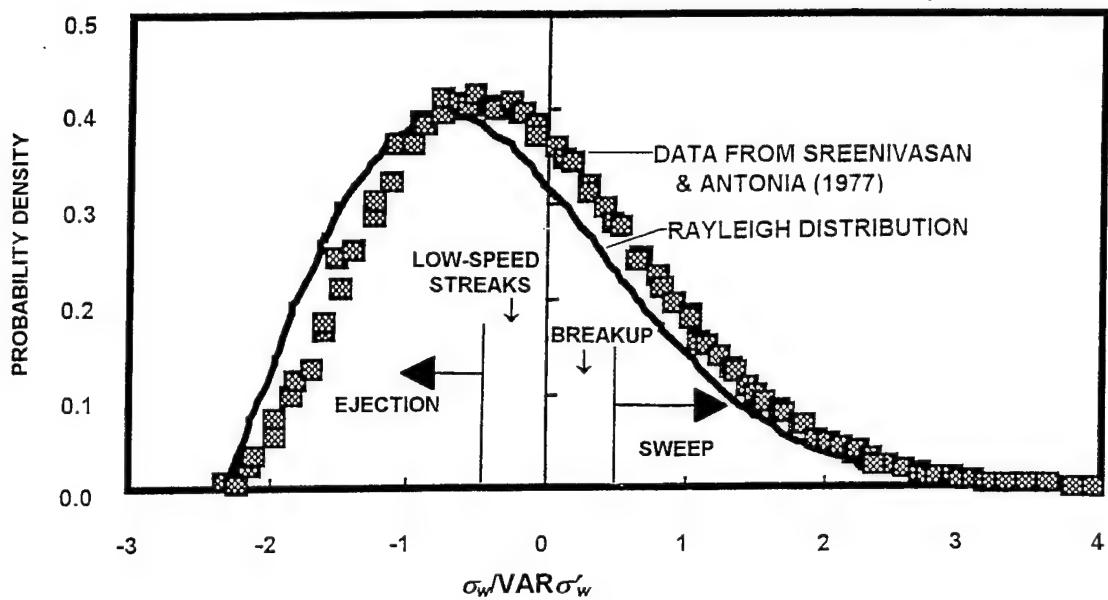
*Figure 17. Demarcation of Microturbulent States on PDF
of Wall Shear Stress Fluctuation*
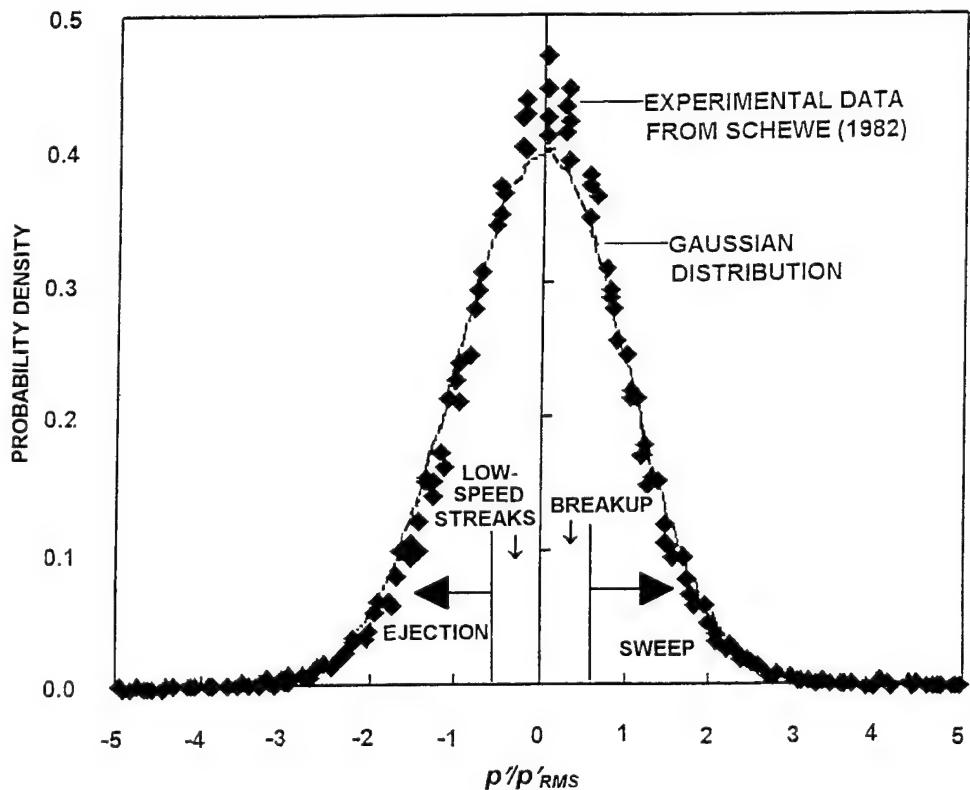
*Figure 18. Demarcation of Microturbulent States on PDF
of Wall Pressure Fluctuation*
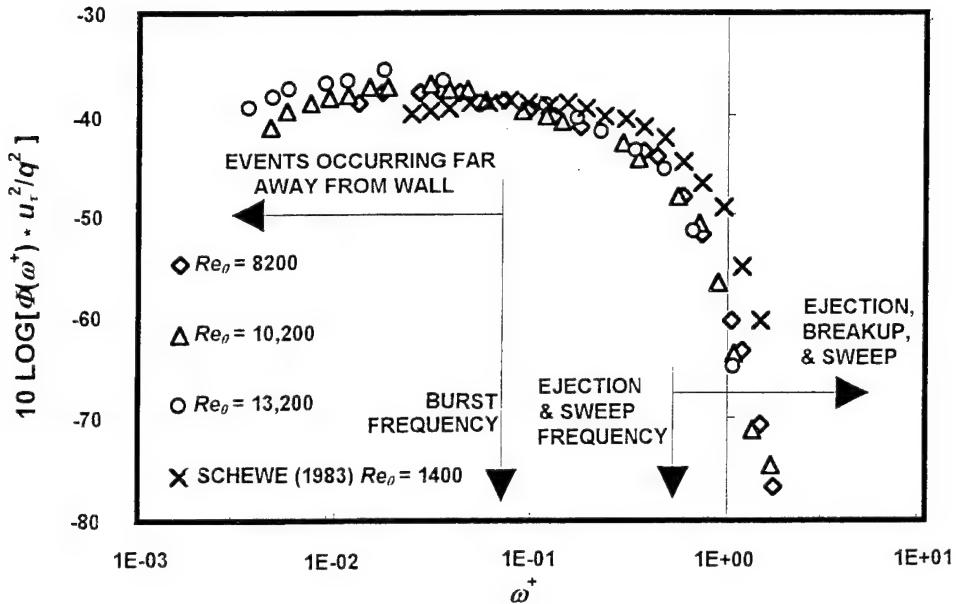
Figure 19. Normalized Smooth Wall Pressure Spectrum in Wall Units

After several T_B periods, the current state is estimated by comparing the shear stress and wall pressure fluctuations with the established PDFs. Then, solutions to the unsteady state probability equations are applied to estimate the state probability of the sensor location and determine the probability of current location within the next time step. The time step is limited by the lower bound of peak frequency $\omega^+ \approx 0.52$, the upper bound of $\omega^+ \approx 0.06$, and the desired accuracy. One rule of thumb is to resolve the highest frequency with six intermediate time steps, which translates into a stepping frequency of $\omega^+ \approx 3$. Selection of the time step must balance the computational load and the accuracy desired.

After the next state probabilities are obtained, a decision has to be made as to whether any external field is to be applied. This is the predictor step. For example, if the current state is low-speed streak and is moving toward sweep, then a normal Lorentz pressure gradient would be applied against the incoming high-momentum fluid motions. If the local state is currently ejection and is moving into breakup, then a decision would be made not to apply any Lorentz pressure gradient, thus letting the low-speed streaks reestablish themselves to maintain the low drag condition. If any external field is to be applied, the overall spatial pattern illustrated earlier in the wall layer turbulence phenomenology would be applied over the entire physical dimension where the external field can be activated. In other words, by using the well-established phenomenology, which has been measured, visualized, and published in the open literature, and which has been thoroughly scrutinized over a Reynolds number range, it is hopeful that only a finitely few sensors would be needed to diagnose the Markov state at the local site and allow the external field to be globally applied with the known spatial pattern. This approach has the potential to greatly reduce the burden on control. Of course, this assumes that our understanding of the turbulent boundary layer physics is further firmly established.

5. A METHOD FOR EMTC IMPLEMENTATION

5.1 SPATIAL PATTERN OF ACTIVE EMTC CELLS

From Emmon's spot configuration and microturbulent measurements, one finds that the spatial pattern of active EMTC cells is nearly invariant with speed, and only the turbulent burst spacing and frequency vary with flow speeds. Therefore, the EMTC strategy is to apply a fixed electrode-magnet pattern, with spacings determined by the highest speed of operation. As the speed increases, more and more EMTC cells are activated in opposing phase; when speed decreases, the polarity of electrodes is reversed to be in-phase over a larger spatial dimension to adjust to the decreasing spatial scales. The electrode-magnet configuration is depicted in figure 20.
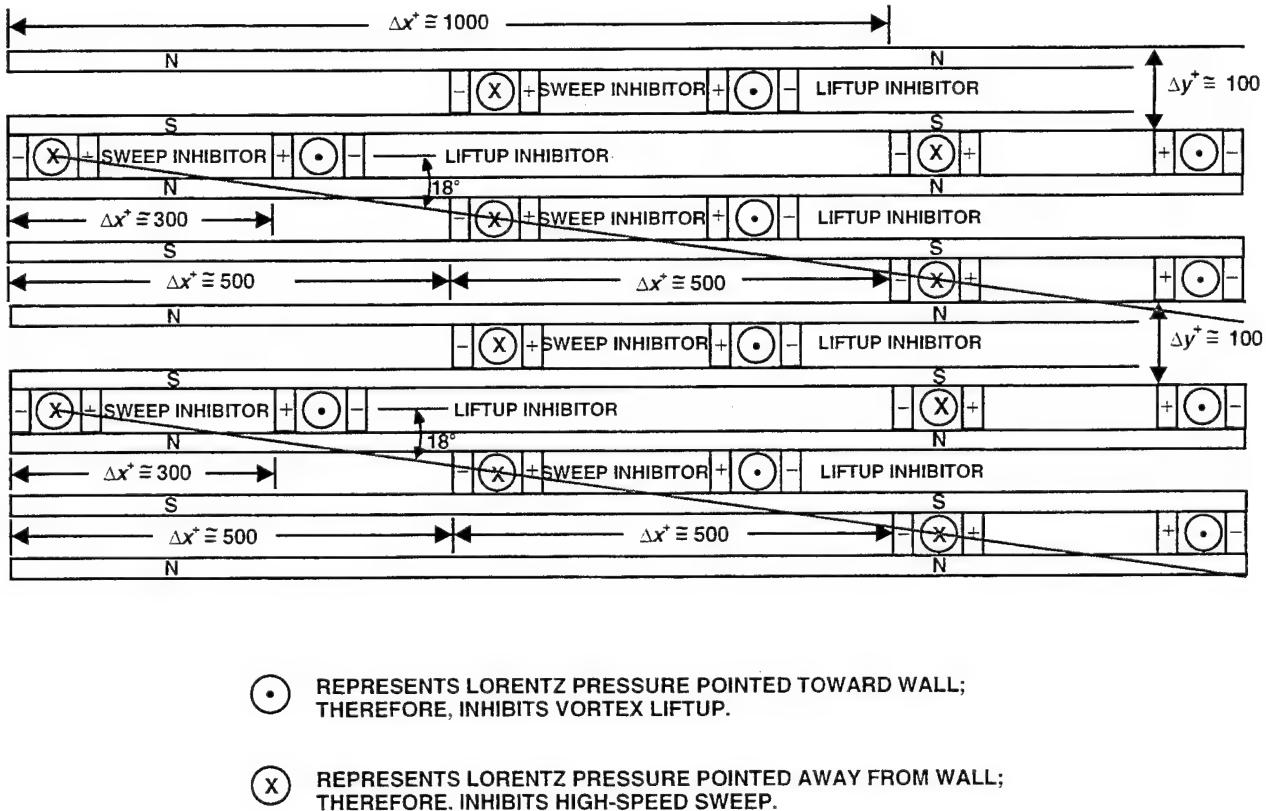

Figure 20. Schematic for Variable-Speed EMTC Based on Simultaneous Cancellation of the Liftup and Sweep Microturbulent Events in the Wall Layer

5.2 TIME DELAY CONTROL OF ACTIVE EMTC CELLS

Given the fixed spatial pattern of the EMTC cells and the known frequency of the burst events, one can selectively activate the electrodes whenever there is a mismatch of the applied fields with the naturally occurring events. These mismatches must be minimized to achieve the turbulence reduction. Using flush-mounted shear stress probes over several diagnostic areas, one can detect the occurrence of burst cycles via the power spectrum and shear stress histogram to determine the time mismatch by using a phase shift key lock circuit. This circuit can be applied to shift the phase until the measured burst frequency is a minimum. This time delay can be considered to be the time shift required to match the fixed pattern with the turbulence production burst cycle.

5.3 FEEDBACK CONTROL

The overall real-time active control is shown in figure 21. The sensors are flush-mounted shear stress and wall pressure probes. The optimal mounting configuration is to be determined later. Sensor outputs are bin-accumulated and spectrally analyzed using digital signal processors to produce PDF's and spectra; they are compared with the base natural state to determine the effects of the applied Lorentz fields. The applied fields can be modulated by the waveform and geometric pattern. The waveform is controlled by the intensity and duration of the applied electric field, and the geometric pattern is controlled by the activation of applied fields at different locations.
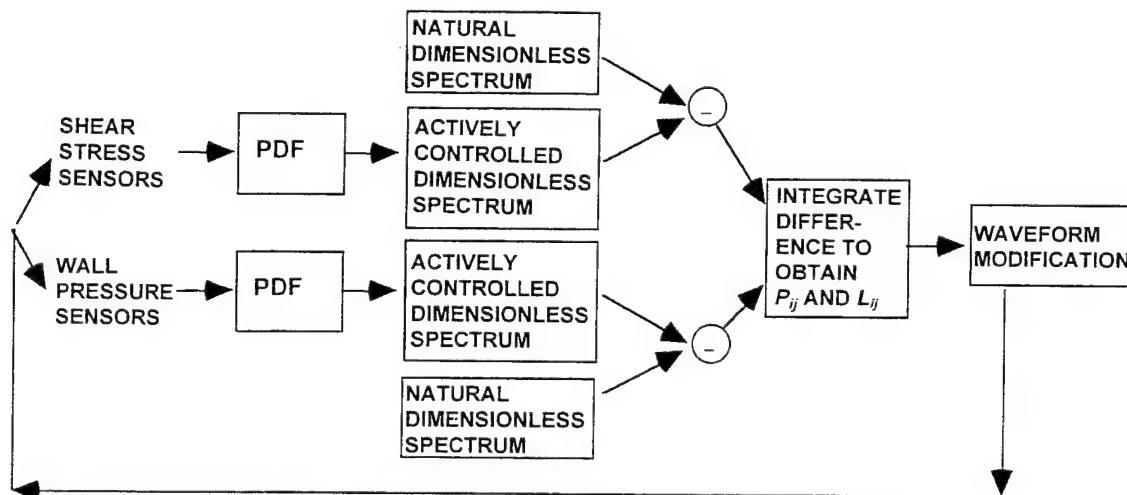

Figure 21. Schematic for Feedback Control

5.4 UNIQUE ADVANTAGES OF MARKOV CONTROL METHODOLOGY

The Markov control methodology offers the following unique advantages:

- It inhibits both the liftup ejections and the sweep simultaneously; therefore, it is more effective in terms of inhibiting turbulence production. This is analogous to the fact that active cancellation of beam vibration is more effective if restraining forces are applied simultaneously to the peak and trough of the beam displacement rather than to the peak only.

- It is a more balanced force system, since no net force is imposed on the flow at any given time.

- It is adaptive to the changing statistics of the turbulence state. The local turbulence state over the diagnosis areas can be detected, and adjusted accordingly, to both the speed and intensity required.

- It requires minimum power input to inhibit the initiation of turbulence vice countering the vortex liftup after it has taken place. This feature has another advantage; because of the nonlinearity of the turbulence, an exact counterforce is not possible to obtain; however, a force to inhibit the initiation of vortex liftup can be determined more accurately; therefore, it may be optimal to apply minimum power rather than the exact amount of power to counter the microturbulent events. This is also necessary due to the fact that the EMTC device's spatial pattern is fixed; if the flow pattern is vastly different from that of the natural state, then the effectiveness of the EMTC device is greatly reduced.

6. SUMMARY AND CONCLUSIONS

From a thorough overview of the published literature of wall layer turbulent events, a conceptual phenomenology of microturbulence, including spatial and temporal patterns of discrete microturbulent events, has been established. An overall, end-to-end, conceptual pictorial representation of the microturbulent events has been constructed. The spatial and temporal patterns of the events invite the concept of controlling microturbulence in such a way that the turbulence-producing events are inhibited while the low-speed streaks, which are considered to be the most stable flow configuration naturally ubiquitous in many turbulent flow conditions beyond the wall turbulence, are preserved.

The repeatable, quasi-periodic, microturbulent events form the deterministic basis on which the Markov process is formulated. For a natural turbulent boundary layer with zero pressure gradient, the simplified Chapman-Kolmogorov equations for the transition probability are solved for the limiting probabilities. These limiting probabilities are related to the experimentally measured arrival rates of the ejection and sweep, which are Poisson processes. For a full four-state model (sweep, ejection, breakup, and low-speed streaks), four arrival rates are needed to completely describe the probability state solution; similarly, for a simplified three-state model (sweep, ejection, and low-speed streaks), three arrival rates are required.

With the presence of externally applied electromagnetic fields, the limiting probabilities no longer apply and the full, unsteady, Chapman-Kolmogorov state probability equations must be solved. The solutions to these linear ordinary differential equations are composed of homogeneous and nonhomogeneous parts. The homogeneous part is of the exponential solution form, with the exponents being eigen-values of the transition probability matrix. The nonhomogeneous part results from the conservation condition of the state probabilities, i.e., they sum to one at all times. The nonhomogeneous solution can also be derived analytically in terms of the homogeneous solution. The initial conditions are satisfied by summing the three eigen-solutions for the four states or the two eigen-solutions for the simplified three-state model. The three-state simplification would be especially useful for high-speed applications where the spatial scales become the width of human hair and the temporal scales so short—into the acoustic frequency range—that the computational power required may exceed present capability.

Lastly, a specific method for EMTC implementation that satisfies all of the known facts of microturbulence phenomenology has been proposed, and time delay and active control flow diagrams determined.

The next step in this work should be to conduct an experiment using the step-by-step approach described above. The experiment must include both quantitative shear stress and wall pressure measurements and flow visualizations with pulsed laser fluorescent dye to determine the effects of the externally applied fields on the naturally occurring turbulence. It is expected that if turbulence is reduced the shear stress and wall pressure fluctuations will be reduced, the coherence of the low-speed streaks will increase, and the burst rate will decrease. Fine tuning of the applied external field intensity and waveforms could result in a turbulence control solution that would have wide engineering application and that would open a new chapter in multidisciplinary fluid mechanics.

7. BIBLIOGRAPHY

Aitchison, J., and J. A. C. Brown (1957), *The Lognormal Distribution*, Cambridge University Press.

Antonia, R. A., and C. W. Van Atta (1977), "Statistical Characteristics of Reynolds Stresses in a Turbulent Boundary Layer," *AIAA Journal*, vol. 15, no. 1, January 1977, pp. 71-75.

Asai, Masahito, and Michio Nishioka (1989), "Origin of the Peak-Valley Wave Structure Leading to Wall Turbulence," *Journal of Fluid Mechanics*, vol. 208, pp. 1-23.

Bakewell, Henry P., Jr, and John L. Lumley (1967), "Viscous Sublayer and Adjacent Wall Region in Turbulent Pipe Flow," *Physics of Fluids*, vol. 10, no. 9, p.188.

Bandyopadhyay, Promode R. (1991), "Comments on Reynolds Number Effects in Wall-Bounded Shear Layers," AIAA Paper 91-0231, American Institute of Aeronautics and Astronautics.

Bandyopadhyay, Promode R. (1982), "Period Bewteen Bursting in Turbulent Boundary Layers," *Physics of Fluids*, vol. 25, no. 10, pp. 1751-1754.

Bandyopadhyay, Promode R., and Anwar Ahmed (1993), "Turbulent Boundary Layers Subjected to Multiple Curvatures and Pressure Gradients," *Journal of Fluid Mechanics*, vol. 246, pp. 503-527.

Bark, F. H. (1975), "On the Wave Structure of the Wall Region of a Turbulent Boundary Layer," *Journal of Fluid Mechanics*, vol. 70, p. 229-250.

Black, T. J. (1966), *Proceedings of the Heat Transfer and Fluid Mechanics Institute*, Stanford University Press, p. 366.

Blackwelder, R. F., and H. Eckelmann (1976), "The Spanwise Structure of the Bursting Phenomenon," in *Structure and Mechanisms of Turbulence I, Lecture Notes in Physics, Vol. 75*, Springer Verlag, New York.

Blackwelder, Ron F., and Helmut Eckelmann (1979), "Streamwise Vortices Associated with the Bursting Phenomenon," *Journal of Fluid Mechanics*, vol. 94, part 3, pp. 577-594.

Blake, William K. (1970), "Turbulent Boundary-Layer Wall-Pressure Fluctuations on Smooth and Rough Walls," *Journal of Fluid Mechanics*, vol. 44, part 4, pp. 637-660.

Brown, G. L., and A. S. W. Thomas, (1977), "Large Structure in a Turbulent Boundary Layer," *Physics of Fluids*, vol. 20, no. 10, part 11, pp. S243-S252.

Cantwell, Brian J. (1981), "Organized Motion in Turbulent Flow," *Annual Reviews in Fluid Mechanics*, vol. 13, pp. 457-515.

Corino, E. R., and R. S. Brodkey (1969), "A Visual Investigation of the Wall Region in Turbulent Flow," *Journal of Fluid Mechanics*, vol. 37, pp. 1-30.

Eckelmann, Helmut (1974), "The Structure of the Viscous Sublayer and the Adjacent Wall Region in a Turbulent Channel Flow," *Journal of Fluid Mechanics*, vol. 65, part 3, pp. 439-459.

Falco, R. E. (1977), "Coherent Motions in the Outer Region of Turbulent Boundary Layers," *Physics of Fluids*, vol. 20, S124.

Gad-el-Hak, Mohamed (1990), "Control of Low-Speed Airfoil Aerodynamics," *AIAA Journal*, vol. 28, no. 9.

Gupta, A. K., J. Laufer, and R. E. Kaplan (1971), "Spatial Structure in the Viscous Sublayer," *Journal of Fluid Mechanics*, vol. 50, part 3, pp. 493-512.

Head, M. R., and P. Bandyopadhyay (1981), "New Aspects of Turbulent Boundary-Layer Structure," *Journal of Fluid Mechanics*, vol. 107, pp. 297-338.

Johansen, J. B., and C. R. Smith (1983), "The Effects of Cylindrical Surface Modifications on Turbulent Boundary Layers," Report FM-3, Department of Mechanical Engineering and Mechanics, Lehigh University, Bethlehem, PA.

Kim, H. T., S. J.Kline, and W. C. Reynolds (1971), "The Production of Turbulence Near a Smooth Wall in a Turbulent Boundary Layer," *Journal of Fluid Mechanics*, vol. 50, part 1, pp. 133-160.

Kline, S. J., W. C. Reynolds, F. A. Schraub, and P. W. Runstadler (1967), "The Structure of Turbulent Boundary Layers," *Journal of Fluid Mechanics*, vol. 30, part 4, pp. 741-773.

Kovasznay, Leslie S. G. (1975), "Turbulent Wakes (Turbulent Shear Flow)," Report ARO-5413-11-E, Johns Hopkins University, Baltimore, MD.

Kreplin, Hans-Peter, and Helmut Eckelmann (1979), "Propagation of Perturbations in the Viscous Sublayer and Adjacent Wall Region," *Journal of Fluid Mechanics*, vol. 95, part 2, pp. 305-322.

Laufer, J., and Narayanan, M.A. B. (1970), "Mean Period of the Turbulent Production Mechanism in a Boundary Layer," *Research Notes*, pp. 182-183.

Löfdahl, L., E. Kälvesten, and G. Stemme (1994), "Small Silicon Based Pressure Transducers for Measurements inTurbulent Boundary Layers," *Experiments in Fluids*, vol. 17, pp. 24-31.

Lu, S. S., and W. W. Willmarth (1973), "Measurements of the Structure of the Reynolds Stress in a Turbulent Boundary Layer," *Journal of Fluid Mechanics*, vol. 60, p. 481.

Mitchell, James E., and Thomas J. Hanratty (1966), "A Study of Turbulence at a Wall Using an Electrochemical Wall Shear-Stress Meter," *Journal of Fluid Mechanics*, vol. 26, part 1, pp. 199-221.

Morrison, W. R. B., K. J. Bullock, and R. E. Kronauer (1971), "Experimental Evidence of Waves in the Sublayer," *Journal of Fluid Mechanics*, vol. 47, part 4, pp. 639-656.

Murlis, J., H. M. Tsai, and P. Bradshaw (1982), "The Structure of Turbulent Boundary Layers at Low Reynolds Numbers," *Journal of Fluid Mechanics*, vol. 122, pp. 13-56.

Nakagawa, Hiroji, and Iehisa Nezu (1981), "Structure of Space-Time Correlations of Bursting Phenomena in an Open-Channel Flow," *Journal of Fluid Mechanics*, vol. 104, pp. 1-43.

Offen, G. R., and S. J. Kline (1974), "Combined Dye-Streak and Hydrogen-Bubble Visual Observations of a Turbulent Boundary Layer," *Journal of Fluid Mechanics*, vol. 62, part 2, pp. 223-239.

Purtell, L. P., P. S. Klebanoff, and F. T. Buckley (1981), Turbulent Boundary Layers at Low-Reynolds Numbers," *Physics of Fluids*, vol. 24, pp. 802-811.

Rajaee, Mojtaba, and Sture K. F. Karlsson (1992), "On the Fourier Space Decomposition of Free Shear Flow Measurements and Mode Degeneration in the Pairing Process," *Physics of Fluids A*, vol. 4, no. 2.

Rajaee, Mojtaba, and Sture K. F. Karlsson (1990), "Shear Flow Coherent Structures via Karhunen-Loève Expansion," *Physics of Fluids A*, vol. 2, no. 12.

Rao, K. Narahari, R. Narasimha, and M. A. Badri Narayanan (1971), "The 'Bursting' Phenomenon in a Turbulent Boundary Layer," *Journal of Fluid Mechanics*, vol. 48, part 2, pp 339-352.

Sabry, A. S., and J. T. C. Liu (1991), "Longitudinal Vorticity Elements in Boundary Layers: Nonlinear Development from Initial Görtler Vortices as a Prototype Problem," *Journal of Fluid Mechanics*, vol. 231, pp. 615-663.

Savage, H. T., W. L. Ditto, P. A. Braza, M. L. Spano, S. N. Rauseo, and W. C. Spring III (1990), "Crisis-Induced Intermittency in a Parametrically Driven, Gravitationally Buckled, Magnetoelastic Amorphous Ribbon Experiment," *Journal of Applied Physics*, vol. 67, no.9.

Schewe, Günter (1983), "On the Structure and Resolution of Wall-Pressure Fluctuations Associated with Turbulent Boundary-Layer Flow," *Journal of Fluid Mechanics*, vol. 134, pp. 311-328.

Sirmalis, J. E. (1976), "A Study of the Drag Characteristics and Polymer Diffusion in the Boundary Layer of an Axisymmetric Body," NUSC Technical Report 4860, Naval Underwater Systems Center, Newport, RI.

Smith, C. R., and S. P. Metzler (1983), "The Characteristics of Low-Speed Streaks in the Near-Wall Region of a Turbulent Boundary Layer," *Journal of Fluid Mechanics*, vol. 129, pp. 27-54.

Smith, C. R., and S. P. Schwartz (1983), "Observations of Streamwise Rotation in the Near-Wall Region of a Turbulent Boundary Layer," *Physics of Fluids*, vol. 26, no. 3.

Sreenivasan, K. R., and R. A. Antonia (1977), "Properties of Wall Shear Stress Fluctuations in a Turbulent Duct Flow," *Journal of Applied Mechanics, Transactions of the ASME*, September 1977, p. 389.

Subramanian, C. S., S. Rajagopalan, R .A. Antonia, and A. J. Chambers (1982), "Comparison of Conditional Sampling and Averaging Techniques in a Turbulent Boundary Layer," *Journal of Fluid Mechanics*, vol. 123, pp. 335-362.

Tiederman, William G., and Thomas S. Luchik (1982), "Wall Layer Structure and Drag Reduction," Report PME-FM-82-2, School of Mechanical Engineering, Purdue University, Lafayette, IN.

Vukoslavcevic, Petar, James M. Wallace, and Jean-Louis Balint (1991), "The Velocity and Vorticity Fields of a Turbulent Boundary Layer, Part 1. Simultaneous Measurement by Hot-Wire Anemometry," *Journal of Fluid Mechanics*, vol. 228, pp. 25-51.

Wallace, J. M., H. Eckelmann, and R. S. Brodkey (1972), "The Wall Region in Turbulent Shear Flow," *Journal of Fluid Mechanics*, vol. 54, p. 39.

Wygnanski, I., M. Sokolov, and D. Friedman (1976), "On a Turbulent 'Spot' in a Laminar Boundary Layer," *Journal of Fluid Mechanics*, vol. 78, part 4, pp. 785-819.

Zakkay, V., V. Barra, and K. Hozumi (1971), "Turbulent Boundary Layer Structure at High and Low Subsonic Speeds," in *Turbulent Boundary Layers—Experiments, Theory, and Modelling*, AGARD Conference Preprint 271, pp. 4-1 - 4-20.

INITIAL DISTRIBUTION LIST

Addressee	No. of Copies
Assistant Secretary of the Navy (RD&A)	1
Undersecretary of Defense (A&T)	1
Defense Intelligence Agency	1
Defense Technical Information Center	12
Advanced Research Projects Agency (Attn: Gary Jones/MSTO)	1
Chief of Naval Operations (Codes N87, N091)	2
Chief of Naval Research (ONR-322--P. Purtell, S. Lekoudis)	2
Naval Sea Systems Command (PEO-SUB-R)	1
Naval Research Laboratory (Attn: Technical Library)	1
Naval Postgraduate School (Attn: Technical Library)	1
Applied Physics Laboratory, Johns Hopkins University	1